III Strong force

8 Unveiling the particle zoo

The timeline of particle discoveries span just over a century for the fundamental SM particles and various composite states called hadrons, shown in figure 45. Particularly striking in this history is a plethora of particles that appeared in experiments around the late 1940s to mid-1960s. The pion was widely anticipated as the mediator of the strong nuclear force, the kaons were more peculiar and the greatest surprise was the sheer multitude of ostensibly fundamental particles appear in experiments. This triggered detailed characterisation of their properties, inspiring the designation of *particle zoo*. This eluded deeper organising principles until the quark model of mesons and baryons comprising up, down, strange quarks. In the 1970s, new resonances yielded evidence for the charm and bottom quarks alongside the gluon. This was the decade many aspects of what we now know as the Standard Model fell into place.

It became clear that this remarkable richness of states was evidence for a single theory of the strong force, quantum chromodynamics (QCD), which is the subject of this chapter. The top quark discovery was widely anticipated but would wait until the mid-1990s. Hadrons remain an active area of research in the 21st century, as the Large Hadron Collider continues to discover new exotic states comprising four or even five quarks (tetraquarks and pentaquarks).

8.1 Nuclear magnetic moments

Early on in the 1930s, mysterious measurements of the proton and neutron magnetic moments revealed the first indirect evidence that they were not fundamental Dirac fermions. The expectation from Dirac theory is that electrically charged point-like spin-1/2 particles should have $g = 2$ and neutral particles cannot have a magnetic moment $g = 0$ as they are not electrically charged:

$$g^{\text{Dirac}}_{\text{proton}} = 2, \tag{8.1}$$

$$g^{\text{Dirac}}_{\text{neutron}} = 0. \tag{8.2}$$

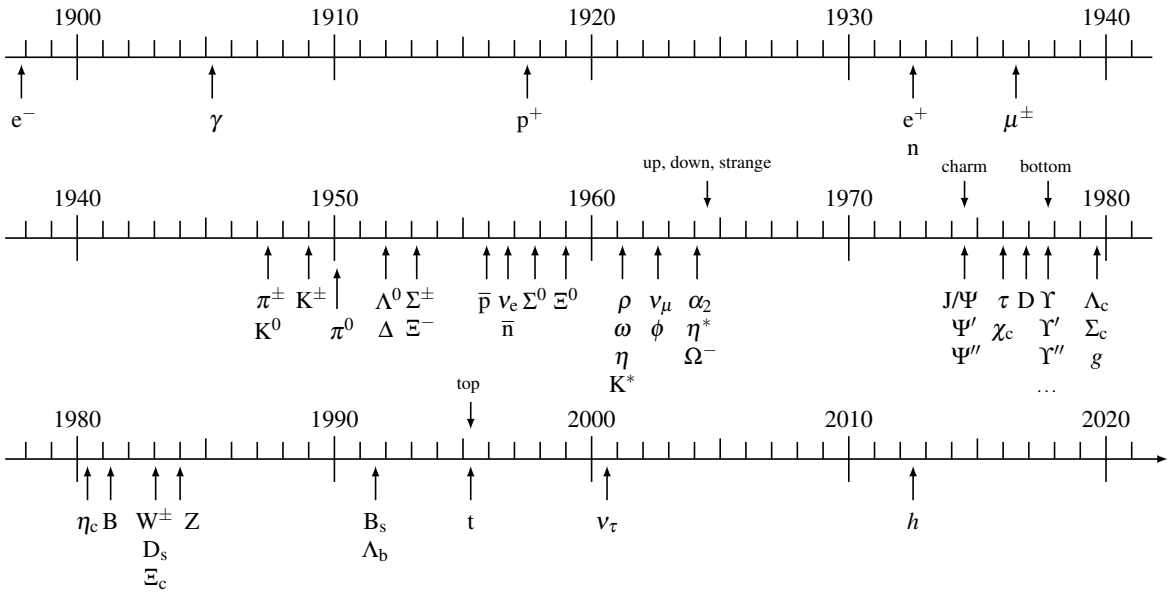

Figure 45: **Timeline of particle discoveries**. Displayed are various fundamental SM particles and composite hadrons. Figure: adapted from Ref. [57]

However, the measured magnetic moments could not be more different, quoting the modern values with uncertainties in parentheses from CODATA [55]:

$$g_{\text{proton}}^{\text{measured}} = +5.585\,694\,689\,3\,(16), \tag{8.3}$$

$$g_{\text{neutron}}^{\text{measured}} = -3.826\,085\,52\,(90). \tag{8.4}$$

This is an utter rejection of Dirac theory. We could imagine some alternative reality where the anomalous magnetic moments were at per-mille like that for the electron e.g. $g^{?}_{\text{proton}} = 2.005, g^{?}_{\text{neutron}} = 0.007$. But for once, nature was refreshingly not even subtle about defying the prevailing Dirac theory. The first measurements revealing a non-zero neutron magnetic moment around 1933 using atomic hyperfine measurements were especially viewed with suspicion. How can an electrically neutral particle possess a magnetic moment? It took several years of experimental development to obtain more accurate and direct measurements to establish the values beyond doubt.

The nuclear magneton μ_N is written in terms of the proton mass

$$\mu_N = \frac{e\hbar}{2m_p}. \tag{8.5}$$

We then express the magnetic moment $\boldsymbol{\mu}$ of a nucleus in terms of the g-factor g and nuclear spin $\mathbf{I}$

$$\boldsymbol{\mu} = g\mu_N \mathbf{I}/\hbar. \tag{8.6}$$

Robert Frisch and Otto Stern discovered the proton magnetic moment in 1933 at Hamburg by deflecting hydrogen through an inhomogeneous magnetic field as in the Stern–Gerlach experiment for electron spin. Already in 1934, the Columbia University group led by Isidor Rabi determined the proton to have unexpectedly large $\mu_p = (3.2 \pm 0.3)\mu_N$ [58] and deuteron unexpectedly small $\mu_d = (0.7 \pm 0.2)\mu_N$ [59] magnetic moments. They developed nuclear magnetic resonance techniques to improve such measurements to per-mille accuracy by 1940, enabling an indirect measurement of the neutron counterpart μ_n:

$$\begin{aligned} \mu_p &= (+2.785 \pm 0.002)\mu_N \\ \mu_d &= (+0.855 \pm 0.002)\mu_N \end{aligned} \quad \Rightarrow \quad \mu_n \approx -2\mu_N. \tag{8.7}$$

Deuterium has spin 1, which implies the the proton and neutron each with spin 1/2 should be aligned $|\uparrow\rangle_p|\uparrow\rangle_n$ so the magnetic moments are additive $\mu_d = \mu_p + \mu_n$. This implies the neutron magnetic moment is around $-2\mu_N$. In 1940, Alvarez and Bloch [60] used the cyclotron at Berkeley to create a beam of free neutrons in an inhomogenous magnetic field, enabling the first direct measurement of the neutron magnetic moment

$$\mu_n = (-1.93 \pm 0.02)\mu_N. \tag{8.8}$$

This was of course the first clue for compositeness, nuclear substructure, and a new fundamental force. This predates the hadron zoo and proposal of quarks that took decades to establish. An important scientific lesson we learn from this is to experimentally test all predictions, even if theory says we should expect to measure nothing, as was the case for the neutron. Today, we now use the magnetic moment of nucleons for medical applications in magnetic resonance imaging.

8.2 Hadrons in nuclear emulsions

A key advance in hadron physics was the invention of nuclear emulsion photographic plates to detect and record energetic charged particles. Marietta Blau developed this method and the plates were manufactured by Ilford and Kodak. Suspended in a thick emulsion on a glass plate are silver halide crystals with heightened concentration to raise particle detection sensitivity. The size of the grains can be smaller than μm, enabling exceptional spatial resolution. When energetic radiation traverses the plate, some of the silver halide crystals along the ionising trajectory turn into silver, which are chemically developed into photographs for permanent record. By counting the grain density, one could determine the ionisation energy loss of the particle.

(a) Kurz's logbook for pion discovery (b) Bristol cosmic-ray group 1949

Figure 46: **Bristol cosmic-ray research group**. Notebook of Marietta Kurz who analysed the photographic emulsions, searching for interesting images and one with her annotation "double meson", the first sign of the pion. From Physics World/Bristol University Special Collections. Right shows Cecil Powell's cosmic-ray research group at Bristol in 1949, photo from CERN Courier **27** (1987) 8.

Charged pions

Cecil Powell assembled a large cosmic-ray research group at the University of Bristol with scanners scouring the photographs under microscopes for interesting particle track events. One such track is shown in figure 46 as logged in the notebook of Marietta Kurz. In many of the landmark discovery papers In 1947, Occhialini and Powell reported the first photos of a pion[43] decaying to a muon. In 1948, specially developed electron-sensitive emulsions were developed by Kodak enabling measurement of the electron from the decaying muon (figure 47). This established the full decay chain of charged particles in the leptonic decays of the pion:

$$\begin{array}{ll} \pi^+ \to \mu^+ + \nu_\mu & \pi^- \to \mu^- + \bar{\nu}_\mu \\ \quad\downarrow & \quad\downarrow \\ \quad\mu^+ \to e^+ + \nu_e + \bar{\nu}_\mu & \quad\mu^- \to e^- + \bar{\nu}_e + \nu_\mu\,. \end{array} \tag{8.9}$$

[43]The June 1997 issue of CERN Courier provides an interesting history of the pion during the 50th anniversary of its discovery https://cds.cern.ch/record/1732689.

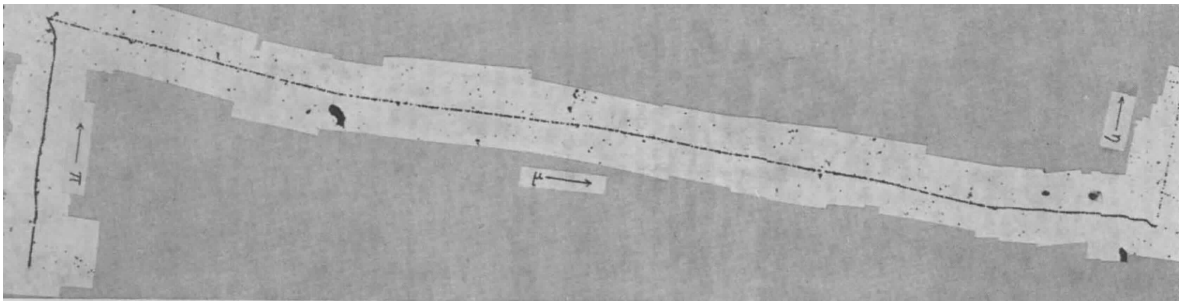

Figure 47: **Charged pion discovery photo**. Historical photographic plate form 1949 showing a charged pion (leftmost line, going up) decaying to muon (long line from left to right) decaying to electron (faint rightmost line, going up) $\pi \to \mu \to e$ (the electron is labelled η in this image). Identified by Rosemary Brown in the Bristol Cosmic Ray Research group, reproduced from Ref. [61].

Kaons

Kaons, or K-mesons, were discovered in a series of cosmic-ray experiments in the Manchester and Bristol groups [44]. Originally, there were neutrals decaying into a pair of charged particles. This gave a distinct "V" fork to the Manchester cloud-chamber tracks shown in figure 48, which was called V^0. Today this corresponds to the neutral kaon with a mass around half that of the proton $m_{K^0} \approx 497.6$ MeV.

Meanwhile, the Manchester group identified charged particles decaying into a charged plus neutral called $\theta^\pm$ while the Bristol group found the three charged pion decay mode named $\tau^\pm$:

$$\theta^\pm \to \pi^\pm \pi^0, \tag{8.10}$$

$$\tau^\pm \to \pi^\pm \pi^\pm \pi^\mp. \tag{8.11}$$

Figure 49 shows a "K track" $\tau^\pm \to \pi^\pm \pi^\pm \pi^\mp$, evidencing a kaon decay from cosmic rays, captured with nuclear emulsion detectors.

The decay signatures were so different that contemporary physicists thought they had discovered different particles. However, what was completely puzzling was that they shared the same mass of around 493.7 MeV and lifetime of around 12.4 ns. Such mysteries were called the "tau–theta puzzle". The particles had other peculiar properties that they dubbed

[44] There is a lovely historical account of this history in a 1997 CERN Courier article entitled *Half a century ago the pion pioneers* https://cds.cern.ch/record/1732677. Rosemary Fowler (nèe Brown) discovered the kaon as a doctoral student in Cecil Fowler's group, published in Nature article 1949 https://www.nature.com/articles/163082a0

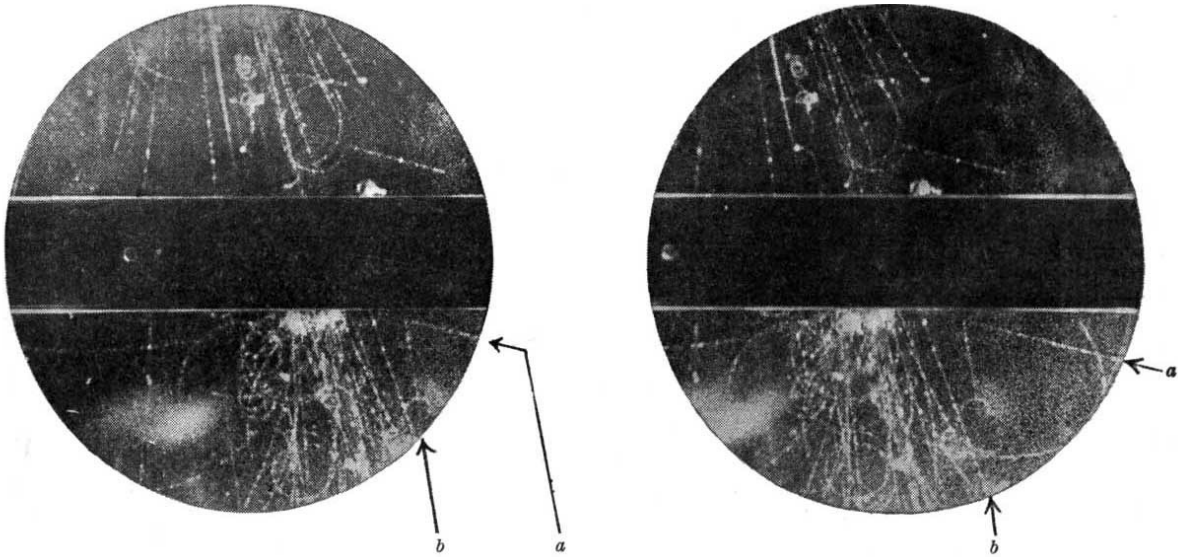

Figure 48: **Manchester kaon discovery photos**. The original caption was: "stereoscopic photographs showing an unusual fork (a b) in the gas by Rochester and Butler at Manchester [62]. The direction of the magnetic field is such that a positive particle coming downwards is deviated in an anticlockwise direction". Neutral particle decaying into two charged pions; a charged particle decaying into a charged pion and a neutral particle.

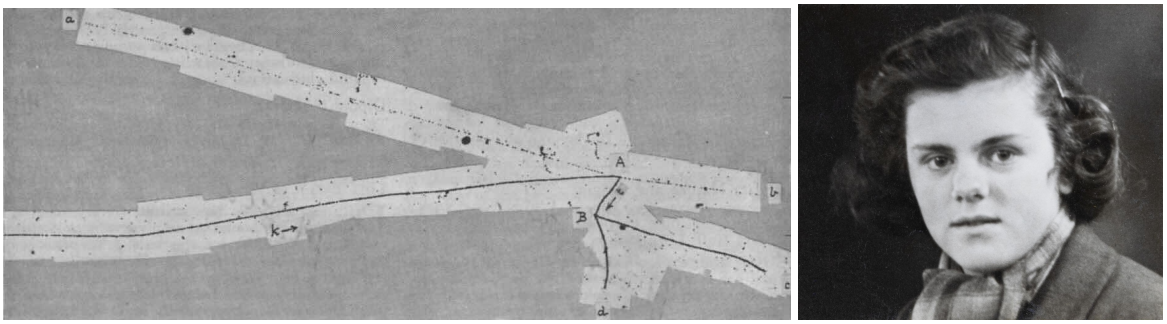

(a) Kaon track (b) Rosemary Brown

Figure 49: **Bristol kaon discovery photo**. Kaon track found by W. J. van der Merwe in a photographic plate: V shaped tracks in cosmic ray from Ref. [61]. Photo showing Rosemary Brown who analysed such events.

"strange", which we shall re-visit in the discussion of the strange quark where the name has stuck. It took a decade to realise the these were the same particles and $\theta^{\pm}, \tau^{\pm}$ are retired in favour of the charged kaon $K^{\pm}$.

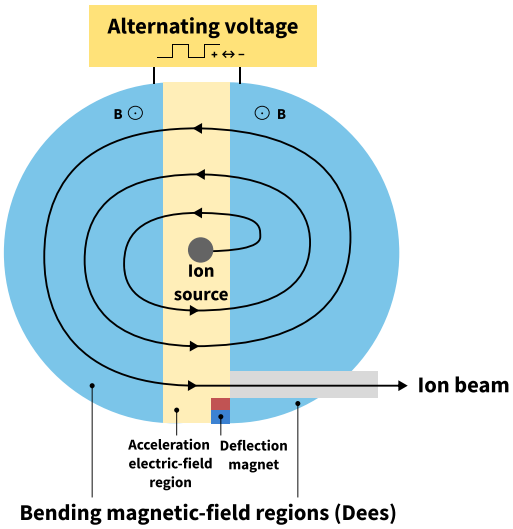

(a) Schematic diagram

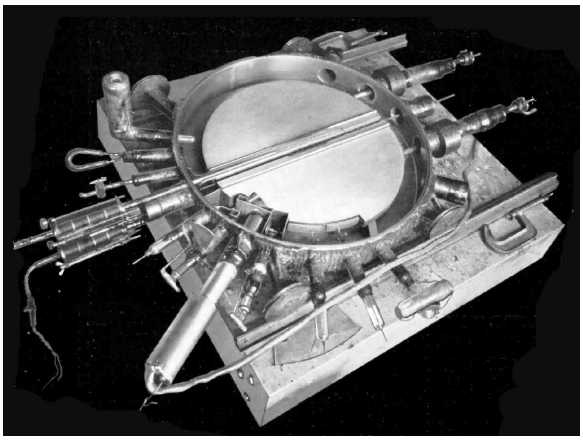

(b) 27 inch cyclotron

Figure 50: **Cyclotron schematic and photo**. Left: schematic diagram of a cyclotron accelerator. Right: the 27 inch cyclotron built by Lawrence and Livingston from John B. Livingood, "Radioactivity by Bombardment" *Electronics* Magazine (1935)

8.3 Cyclotrons to synchrotrons

The deluge of the particle zoo arose from concurrent advances in particle accelerators.

Cyclotron

A more compact alternative to a linear accelerator is to wrap the above setup into a circular geometry to create a circular accelerator, which has a complementary set of advantages and disadvantages. The key idea is to exploit the magnetic part of the Lorentz force to generate a centripetal force mv^2/r via a perpendicular magnetic force of magnitude $f = QvB$:

$$\frac{mv^2}{r} = QvB. \tag{8.12}$$

With the angular speed $\omega = v/r$, we find the **cyclotron frequency** is

$$f = \frac{\omega}{2\pi} = \frac{QB}{2\pi m}. \tag{8.13}$$

The key idea here is that the frequency is independent of the particle velocity. So acceleration only requires an alternating voltage at constant frequency, which is simple to engineer.

A cyclotron comprises two 'D'-shaped objects where the electric polarity oscillates to provide acceleration in the gap. Meanwhile, the magnetic field within each dee ensures particle always experiences a centripetal force towards the same centre turning the particle. The source of particles are injected at the centre and spiral outwards as its velocity and therefore bending radius increases with acceleration. The ions in the accelerating region are attracted to one of the Dees. A final deflection magnet then allows the particle to exit at a well-defined energy.

Ernest Lawrence and Stanley Livingston constructed the first cyclotron[45] at Berkeley, California in 1931 (figure 50). Reaching 1 MeV allowed reproducing the Cockcroft–Walton experiment that split the atom at Cambridge. This new class of machine saw rapid progress, reaching around 20 MeV by the end of the 1930s. By such energies, the mass of the proton receives noticeable relativistic correction from the gamma factor $\gamma = E/m$. From equation (8.13), we see that to maintain constant frequency for the alternating voltage, we can steadily ramp up the magnetic field B to compensate for the increasing m. This modification to synchronise the magnetic field with particle energy goes by the name of **synchro-cyclotron**.

In 1948, the first synchro-cyclotron machine at Berkeley reached a colossal (for the time) 184 inches in size and weighed 10^7 kg, accelerating alpha particles from 380 MeV to 720 MeV. The was technologically possible thanks to the invention of phase stability in V. Vecksler and independently by E. Macmillan, where successive beam focusing and de-focusing allows stable orbits. Remarkably, such singular focus on increasing cyclotron energy meant nobody added a detector until Lattes moved from Powell's Bristol group to Berkeley and suggested placing photographic emulsions to image collision debris from such a powerful machine. The beam energies of 380 MeV were enough to create the charged pions in great abundance earlier observed by the British cosmic-ray groups. The neutral pion π^0 was more difficult to find as it is electrically and does not appear in photographic emulsions. The neutral pion decays electromagnetically via its hallmark di-photon signature with a branching ratio of 99.8%:

$$\pi^0 \to \gamma\gamma, \quad m_\pi = 135 \text{ MeV}. \tag{8.14}$$

The neutron pion was discovered at Berkeley in 1950 by Panofsky, Steinberger, and Steller.

Today, there are thousands of active cyclotrons around the world that benefit the human condition. Many of these are in hospitals, producing indispensable radioisotopes for medical imaging including Positron Emission Tomography (PET). They are also now used for

[45] As often in history, the Nobel prize recognising such groundbreaking research went to Lawrence, but not Livingston who was a graduate student at the time.

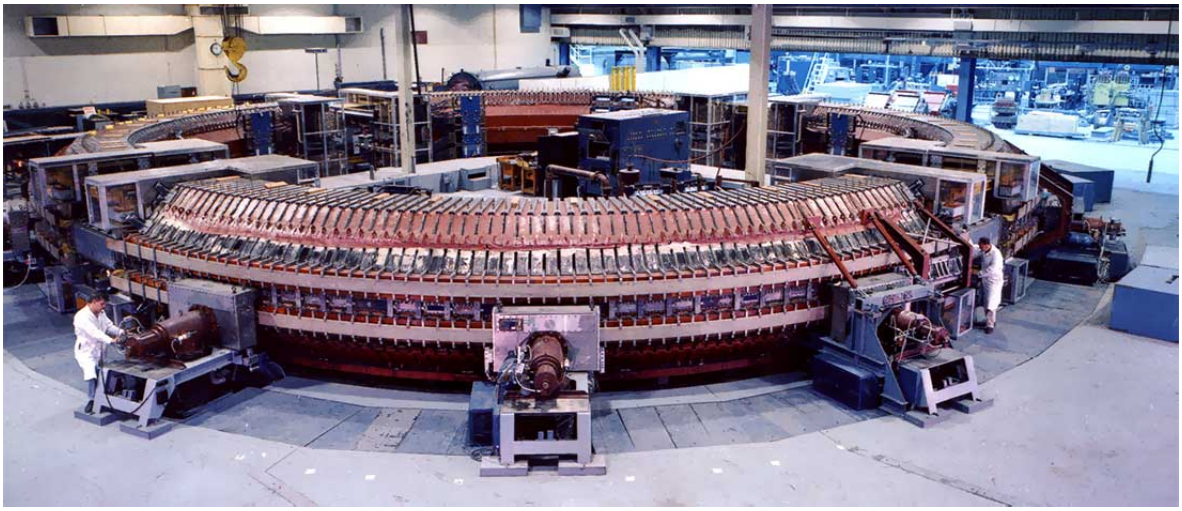

Figure 51: **Brookhaven Cosmotron**. BNL, a synchrotron operated in 1952–1966.

cutting-edge proton therapy, where a cyclotron accelerates protons to destroy cancerous cells with reduced dose to surrounding healthy tissue via the Bragg peak technique. Indeed, there are several cyclotrons in New York City, including the NYU Department of Radiology[46] and New York Proton Center[47]. These are beautiful examples of how a research breakthrough for fundamental physics later finds applications that routinely save human lives. Nonetheless, these devices are large and expensive, occupying very large rooms and costing $\gtrsim 10^7$ dollars. Perhaps you will be inspired to join accelerator science research not just to create more compact machines for fundamental physics but also make therapies more accessible, affordable and portable for society.

Synchrotron

The synchrotron is an evolution of the synchro-cyclotron such that the bending radius is constant. This combines electric field regions for increasing particle energy and bending to steer particles in such a way that it is synchronised to the particle energy. The main downside is synchrotron radiation, which is a consequence of Maxwell's equation that all accelerated charges emit electromagnetic radiation. The power emitted P by a charged particle radiates in one revolution is given by Larmour's formula

$$P = \frac{2}{3}\frac{e^2}{4\pi\varepsilon_0 mc^2}\frac{m}{\rho^2}\left(\frac{E}{m}\right)^4 \propto \frac{E^4}{m^4}\frac{1}{\rho^2}. \tag{8.15}$$

[46] https://med.nyu.edu/departments-institutes/radiology/research
[47] https://www.nyproton.com/about-proton-therapy

Here, m and e are the mass and charge of the particle being accelerated, ρ is the radius of curvature and E is the energy of the particle. Combating synchrotron radiation requires as large a radius as possible. Synchrotrons involving heavier particles also result in reduced comparative radiated emission, justifying proton colliders over electron colliders having higher centre-of-momentum energies. From equation (2.13) $R/\mathrm{m} = (pc/\mathrm{GeV})/[0.3(B/1\ \mathrm{T})]$, we find the momentum and magnetic field sets the bending radius and thus size of a circular accelerator.

The Cosmotron at Brookhaven National Laboratory (figure 51) opened in 1952 and accelerated protons up to 3 GeV. Berkeley built the Bevatron two years later and reached up to 7 GeV.

8.4 Bubble chamber

The bubble chamber is a spiritual successor to the cloud chamber and was a key detector technology in particle physics discoveries invented by D. Glazer and L. Alvarez in the 1950s. While particle tracks appear from condensation in cloud chambers, the bubble chamber inverts this phase transition such that charged particles trigger the liquid to boil into gas bubbles. The main benefit is the higher material density offered by liquid compared to gas to increase interaction probability. The liquid can act as both target and detector, with hydrogen being a proton target and deuterium having neutrons, while heavier atomic materials are more suited to neutrino detection.

Figure 52a shows a schematic diagram of the bubble chamber detection process. The steps to detection are as follows:

Beam arrives → Piston expands → Liquid superheated → Beam strikes liquid → Particles produced → Tracks of bubbles

Originally, liquid hydrogen was used, which has a boiling point of 20.3 K at 1 atmosphere pressure, requiring sophisticated cryogenics and safety interlocks. The liquid is kept under pressure just below its boiling point and the moment before the beam arrives, a piston relaxes to lower the pressure. This causes the liquid to become *superheated*, meaning its temperature is above the boiling point but remains in its liquid phase. As charged particles traverse this superheated liquid, the ionization triggers the boiling process to leave a tracks bubbles with high spatial resolution. Cameras surrounds the bubble chambers to capture the tracks bending inside a magnetic field, allowing particle charge and momentum measurements.

Figure 52b shows the Big European Bubble Chamber together with its piston at the CERN Microcosm exhibit (figure 52c), the last and largest such detector to have operated

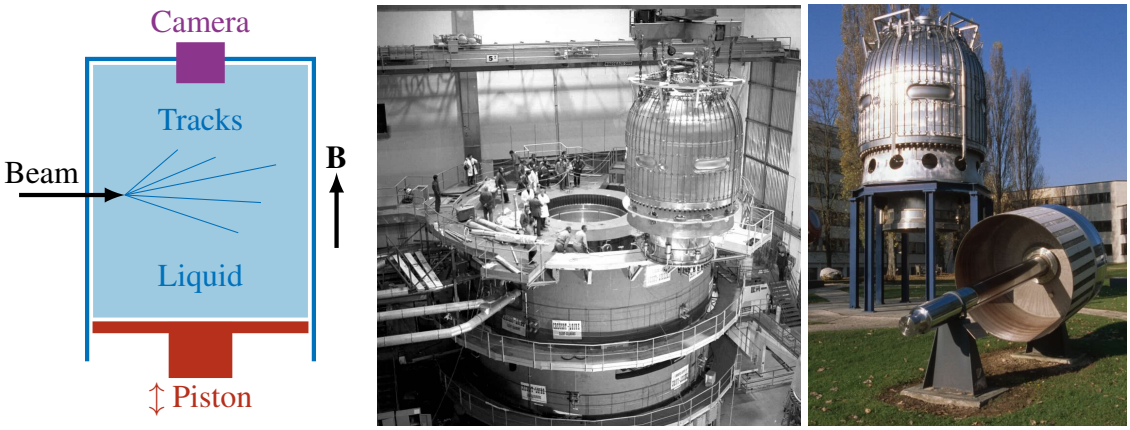

(a) Schematic sketch (b) Installation into cryostat (c) Piston

Figure 52: **Bubble chamber schematic and photos**. Schematic sketch shows the principle of operation for a bubble chamber. The photos display the Big European Bubble Chamber (BEBC) at CERN. (b) Installation into the cryostat in 1971 CERN. (c) Piston in front of the bubble chamber at the CERN Microcosm museum CERN-PHOTO-SIS-68681.

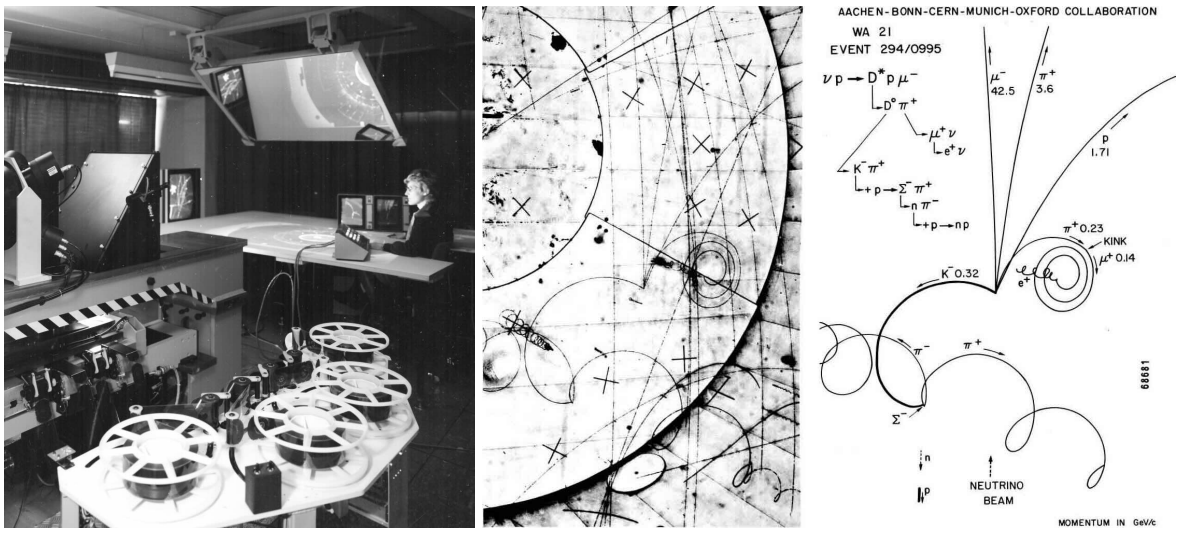

(a) Scanning film photos (b) D-meson bubble chamber tracks

Figure 53: **Analysing Big European Bubble Chamber (BEBC) data**. Madeleine Znoy using the Electron RAy Scanning and Measuring Equipment (ERASME) film scanner imaging BEBC events CERN. Event showing D-meson production and decay from neutrino beam from WA21 experiment CERN-PHOTO-SIS-68681.

during the 1970s. Human scanners had to sift through the cornucopia of film photographs in projectors (figure 53a) and initially the tracks are manually traslated onto cards. The exquisite spatial resolution of the bubble chamber and sensitivity to charged particles were the key advantages of this technology (figure 53b). The main downside of this detector technology was the relatively large time required to reset the detector after each image is taken, given this requires resetting the piston.

During this period 1960–70s, automation developed rapidly in parallel to electronic computers aiding spatial measurement of photographed tracks. During the 1980s, bubble chambers retired in favour of electronic readout capabilities of spark chambers and semiconductor sensors that would become the de facto standard for charged-particle tracking. Bubble chambers are now museum pieces as monuments of scientific discovery, scattered across particle physics laboratories such as Fermilab and CERN.

9 Quarks and hadrons

We now study some of the phenomenological organising principles underlying the particle zoo of quarks and hadrons. Quarks[48] are proposed as the matter constituents of nucleons. The modern interpretation is that they are a set of elementary fermions with spin-$\frac{1}{2}$ that interact via the **strong force**. There are six **flavours** of quarks paired into three generations:

$$\begin{pmatrix} u \\ d \end{pmatrix}, \quad \begin{pmatrix} c \\ s \end{pmatrix}, \quad \begin{pmatrix} t \\ b \end{pmatrix}. \tag{9.1}$$

called up, down, charm, strange, top and bottom quarks respectively. Their antiparticle partners are denoted by overbars. Table 1 presents all the quantum numbers: charge (Q), strangeness (S), charm (C), bottomness (B), topness (T), and their masses (m) of all known quarks.

9.1 How to build a hadron

We now construct some hadrons using the lightest quarks: up and down. Free quarks are never directly observed. We instead find them as bound states called **hadrons**, which we call mesons and baryons[49], according to their quark content:

[48] Merriam Webster provides an interesting discussion of the etymology and pronunciation of *quark*. I pronounce *quark* rhyming with *mark* as used in "Three quarks for Muster Mark!" from James Joyce's *Finnegans Wake*, though Murray Gell-Mann originally rhymed it with *fork*.

[49] The etymology comes from Greek *mesos* meaning middle and *barýs* meaning heavy, which are helpful to remember that baryons have higher quark content than mesons.

Quark	Symbol	Q [e]	S	C	B	T	m [GeV]
Down	d	$-\frac{1}{3}$	0	0	0	0	<1
Up	u	$+\frac{2}{3}$	0	0	0	0	<1
Strange	s	$-\frac{1}{3}$	-1	0	0	0	<1
Charm	c	$+\frac{2}{3}$	0	1	0	0	≈ 1.3
Bottom	b	$-\frac{1}{3}$	0	0	-1	0	≈ 4.3
Top	t	$+\frac{2}{3}$	0	0	0	1	≈ 174

Table 1: Quantum numbers and masses of known quarks. For antiquarks, invert the sign of all the quantum numbers. Q: electric charge, S: strange number, C: charm number, B: bottom number, T: top number.

Meson	Quark content	J^P	Q [e]	Rest mass [MeV]
π^+	$u\bar{d}$	0^-	+1	139.57018 (35)
π^0	$u\bar{d}$ or $d\bar{u}$	0^-	0	134.9766 (6)
π^-	$d\bar{u}$	0^-	−1	139.57018 (35)
ρ^+	$u\bar{d}$	1^-	+1	775.4 (4)
ρ^0	$u\bar{d}$ or $d\bar{u}$	1^-	0	775.49 (34)
ρ^-	$d\bar{u}$	1^-	−1	775.4 (4)

Table 2: The lightest mesons of spin-0 (π) and spin-1 (ρ).

- **Mesons**: integer spin states composed of a quark and an antiquark $q\bar{q}$.
- **Baryons**: half-integer spin states composed of three quarks qqq.
- **Antibaryons**: half-integer spin states composed of three antiquarks $\bar{q}\bar{q}\bar{q}$.

In recent years, experiments such as LHCb at CERN have discovered more exotic states comprising four (tetraquarks $q\bar{q}q\bar{q}$) and even five (pentaquarks $qqqq\bar{q}$) quarks[50]. We shall not discuss them, but they are an interesting active field of research.

Parity By convention, quarks have parity $P_q = +1$ while antiquarks $P_{\bar{q}} = -1$. The general prescription for calculating parity of a hardon is to multiply the parities of the individual quarks/antiquarks with the orbital angular momentum L. For mesons and baryons respectively, this gives

$$\begin{aligned} P_{\text{meson}} &= P_q P_{\bar{q}} (-1)^L = (-1)^{L+1} \\ P_{\text{baryon}} &= P_{q_1} P_{q_2} P_{q_3} (-1)^L = (-1)^L \end{aligned} \tag{9.2}$$

We usually denote the final angular momentum J (usually $J = S$ as we consider $L = 0$ states) and parity $P = \pm 1$ states together in the compact notation J^P.

Mesons Consider first the mesons whereby we couple two spin-$\frac{1}{2}$ particles – a quark and an antiquark. The lightest spin-0 states correspond to **pions** while the spin-1 states are **rho mesons** (table 2). The pions with $J^P = 0^-$ is sometimes called a **pseudoscalar**.

Baryon	Quark content	J^P	Q [e]	Rest mass [MeV]
p	uud	$\frac{1}{2}^+$	+1	938.272046 (21)
n	udd	$\frac{1}{2}^+$	0	939.565378 (21)
Δ^{++}	uuu	$\frac{3}{2}^+$	+2	1 232 (2)
Δ^+	uud	$\frac{3}{2}^+$	+1	1 232 (2)
Δ^0	udd	$\frac{3}{2}^+$	0	1 232 (2)
Δ^-	ddd	$\frac{3}{2}^+$	−1	1 232 (2)

Table 3: The lightest baryons of spin-$\frac{1}{2}$ (p,n) and spin-$\frac{3}{2}$ (Δ)

Baryons We now couple three quarks together. The spin-$\frac{1}{2}$ states correspond to our familiar nucleons while the spin-$\frac{3}{2}$ states are Delta baryons of slightly higher mass (table 3).

With this quark model involving up and down quarks, we can understand reactions involving the formation of pions:

$$\begin{aligned} p \quad + \quad p \quad \rightarrow \quad p \quad + \quad p \quad + \pi^+ + \pi^- \\ (uud) + (uud) \rightarrow (uud) + (uud) + (u\bar{d}) + (d\bar{u}) \end{aligned} \tag{9.3}$$

We can also follow the quarks during resonant production of a Delta baryon:

$$\begin{aligned} p \quad + \quad \pi^- \rightarrow \quad \Delta^0 \quad \rightarrow \quad n \quad + \pi^0 \\ (uud) + (d\bar{u}) \rightarrow (udd) \rightarrow (udd) + (u\bar{u}) \end{aligned} \tag{9.4}$$

Every quark/antiquark has a baryon number of $\frac{1}{3}/-\frac{1}{3}$. We make an important observation:

Total baryon number and **quark flavour** are conserved in strong interactions.	(9.5)

9.2 Strangeness and kaons

In the late 1940s, the Manchester and Bristol cosmic-ray groups observed new hadronic particles. One type was the kaon $K^\pm$ which was produced by a strong interaction:

$$p + p \rightarrow p + p + K^+ + K^- \tag{9.6}$$

Peculiarities arise when we examine the decay of a kaon. One decay mode with branching ratio of 0.21 is

$$\begin{aligned} K^+ \quad &\rightarrow \pi^+ + \pi^0 \\ (u\bar{d})? \ &\rightarrow (u\bar{d}) + (u\bar{u}) \end{aligned} \tag{9.7}$$

[50] https://cds.cern.ch/record/2814136

By conservation of baryon number, we rule out $K^+ = (uud)$ so kaons must be mesons and we hypothesise $K^+ = (u\bar{d})$. If this were the case, by the strong interaction we expect this to decay with a mean lifetime of order $\sim 10^{-23}$ s. Instead, we observe the mean lifetime of (9.7) to be $\sim 10^{-8}$ s, consistent with the weak interaction.

Gell-Mann and Nishijima resolved this by introducing a new quantum number called strangeness S, which we now attribute to the strange quark s. By (historical) convention, a strange quark s has strangeness $S = -1$ and charge $Q = -1/3$. The kaon formation (9.6) via the strong interaction is now explained by

$$\begin{aligned} p \quad + \quad p \quad &\to \quad p \quad + \quad p \quad + K^+ + K^- \\ (uud) + (uud) &\to (uud) + (uud) + (u\bar{s}) + (\bar{u}s) \\ \text{strangeness}: \quad 0 \qquad 0 \quad &\to \quad 0 \qquad 0 \qquad (+1) \quad (-1) \end{aligned}$$

while the kaon decay (9.7) via the weak interaction reads

$$\begin{aligned} K^+ \quad &\to \quad \pi^+ \quad + \quad \pi^0 \\ (u\bar{s}) \quad &\to (u\bar{d}) + (u\bar{u}) \\ \text{strangeness}: \quad (+1) \quad &\to \quad 0 \qquad 0 \end{aligned}$$

We make the historically important observation about strangeness:

Conservation of strangeness is obeyed in strong but violated in weak interactions.

9.3 Meson & baryon multiplets

Gell-Mann sought order out of the seemingly unwieldy number of mesons and baryons formed from lightest 3 quarks: up, down and strange. We focus on the lightest hadronic states with $L = 0$.

Mesons: figure 54 illustrate using wight diagrams the possible combinations of quark-antiquark $q\bar{q}$ pairings using up, down and strange. There are nine particles where we have the **pseudoscalar** and **vector** meson nonets corresponding to spin-parity $J^P = 0^-$ and 1^- respectively.

Baryons: we can do similar for the baryons giving figure 55. These show the possible combinations of $q_1q_2q_3$ using up, down and strange. We notice the absence of uuu, ddd, sss states in the spin-parity $J^P = \frac{1}{2}^+$ case. We also note there are two states made of uds in the $J^P = \frac{1}{2}^+$ case.

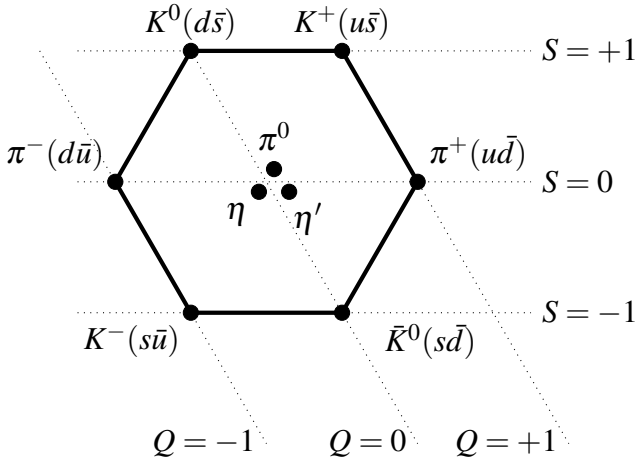

(a) $J^P = 0^-$ meson pseudoscalar nonet.

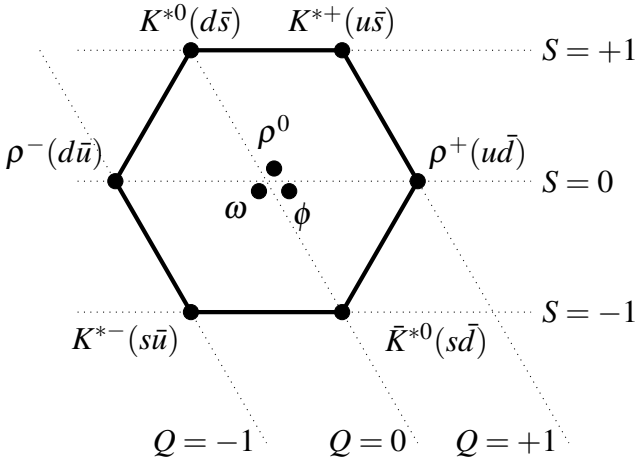

(b) $J^P = 1^-$ meson vector nonet.

Figure 54: **Meson nonets**. This is for spin-parity $J^P = 0^-$ (a) and 1^- (b) composed of up, down and strange quarks and antiquarks. Here, Q and S are charge and strangeness, respectively.

To account for the differences between the $J^P = \frac{1}{2}^+$ and $J^P = \frac{3}{2}^+$ multiplets, we impose the fact that the spin and spatial parts of the baryon wavefunction must be *symmetric* with respect to label exchange. (We note baryons, being fermions, require the total wavefunction to be *antisymmetric*; we resolve this apparent paradox when we acknowledge the existence of an antisymmetric colour wavefunction for the quarks.) In the lowest level $L = 0$, so spatial states are symmetric (even parity $P = (-1)^{L=0} = +1$). So to obtain a symmetric spin-spatial

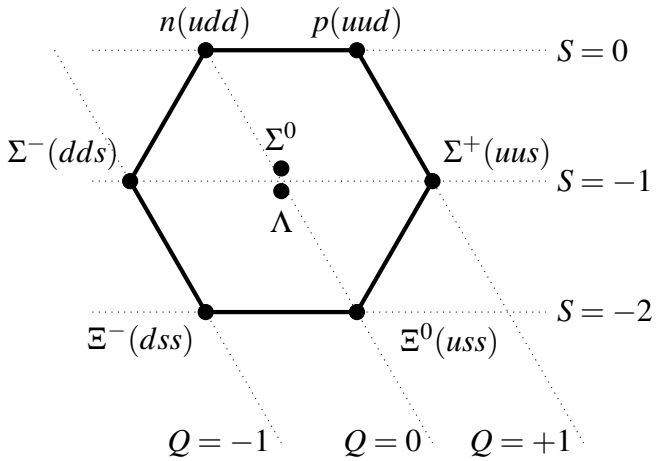

(a) $J^P = \frac{1}{2}^+$ pseudoscalar baryon octet.

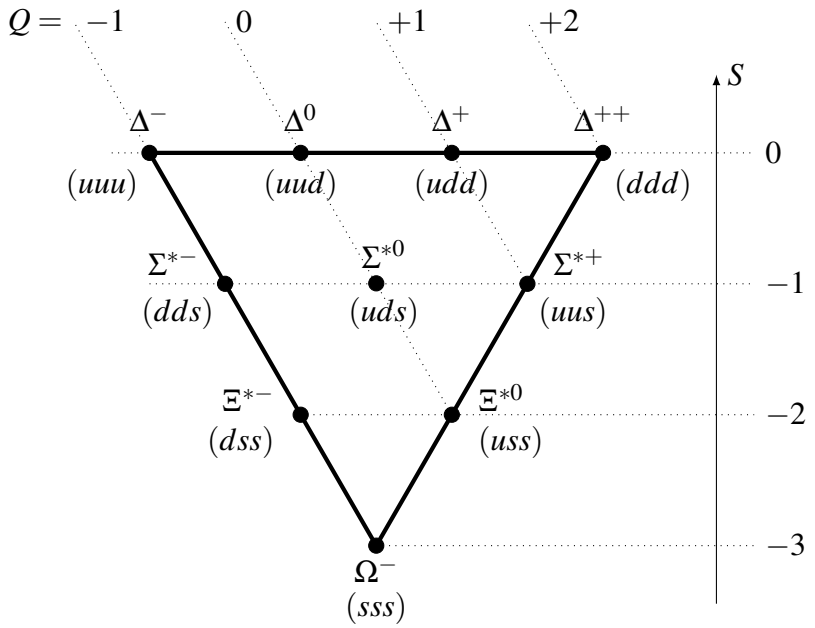

(b) $J^P = \frac{3}{2}^+$ baryon vector decuplet.

Figure 55: **Baryon octet and decuplet**. This is for spin-parity $J^P = \frac{1}{2}^+$ (a) and $\frac{3}{2}^+$ (b) respectively composed of up, down and strange quarks and antiquarks. Here Q and S are charge and strangeness respectively.

state, the spin wavefunction must also be symmetric.

We now consider the possible quark combinations:

- **Two like quarks**: For a pair of identical quarks $q_1 q_1$, the only way to construct a symmetric state is to align their spins i.e. $|\uparrow_1\uparrow_1\rangle$ giving spin-1. By the rules of angular momentum addition, introducing a third quark $q_2 \neq q_1$ to the system gives spin-$\frac{1}{2}$ or spin-$\frac{3}{2}$. So the quark combinations with two like quarks

$$uud,\ uus,\ ddu,\ dds,\ ssu,\ ssd$$

  can be in states $J = \frac{1}{2}$ or $\frac{3}{2}$.

- **Three like quarks**: In the case of all three identical quarks

$$uuu, ddd, sss$$

  the only way to obtain symmetric spin state is for all of their spins to align i.e. $|\uparrow_1\uparrow_1\uparrow_1\rangle$ to give $J = \frac{3}{2}$ only.

- **No like quarks**: For the last case of no like quarks uds, let us consider the pair ud first. We now have two cases:

  1. ud in spin-0 state – adding s results in $J = \frac{1}{2}$ state.
  2. ud in spin-1 state – adding s results in $J = \frac{1}{2}$ of $\frac{3}{2}$ state.

Counting everyone up, we find indeed we have eight $J^P = \frac{1}{2}^+$ states and ten $J^P = \frac{3}{2}^+$ states.

9.4 Colour charge

As suggested by the name quantum chromodynamics (QCD), a defining feature of the strong force is a new type of charge called colour. Every quark possesses one of three **colours charges**, which we can call red r, green g, blue b. Antiquarks posses anticolour: anti-red $\bar{r}$, anti-green $\bar{g}$, anti-blue $\bar{b}$. This is analogous to how electromagnetism has a single electric charge e, such that particles with electric charge feel the electromagnetic force. Colour is a generalisation of this idea where a force can have three distinct charges. Indeed, we could have called this the 'strong force charge' rather than colour. We can explicitly label a quark q with its charge q_i with $i = \{r, g, b\}$ (and antiquarks $\bar{q}_i$ with anticolour $i = \{\bar{r}, \bar{g}, \bar{b}\}$) or as a vector

$$q = \begin{pmatrix} q_r \\ q_g \\ q_b \end{pmatrix}. \tag{9.8}$$

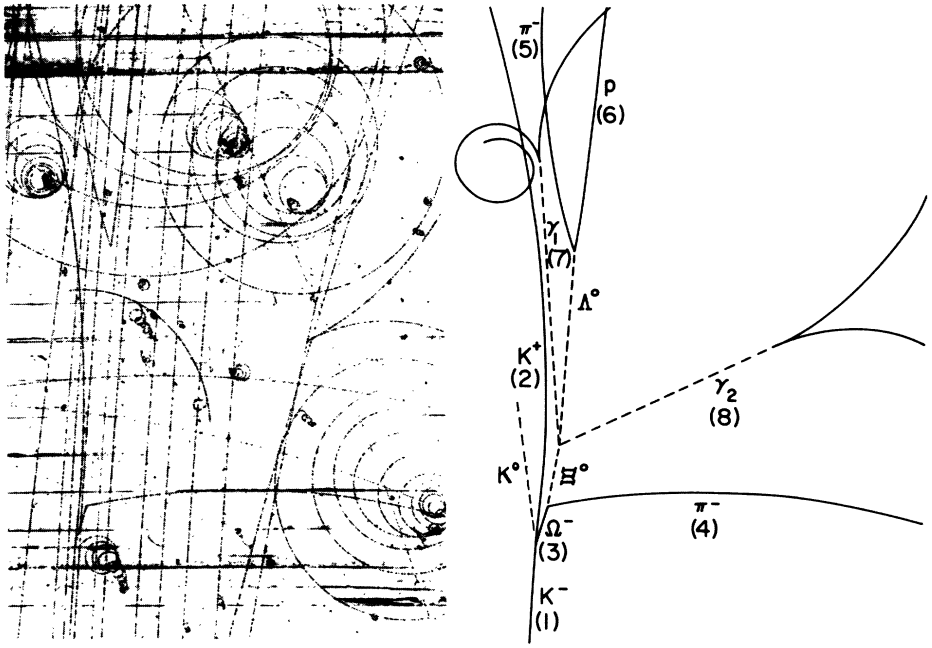

Figure 56: **Triple strange omega baryon discovery** Bubble chamber figure of the Ω^- baryon observed from Ref. [63].

Why introduce yet another quantum number? The historical arguments are interesting in themselves. Colour was motivated by Greenberg in 1964 to ensure hadronic wavefunctions are consistent with the Fermi–Dirac statistics from quantum mechanics, which requires identical fermions to be antisymmetric upon exchange of labels. The total baryon wavefunction comprises spatial, flavour, spin and colour parts:

$$|\Psi\rangle = |\psi_{\text{spatial}}\rangle|\psi_{\text{flavour}}\rangle|\psi_{\text{spin}}\rangle|\psi_{\text{colour}}\rangle \tag{9.9}$$

Let us consider the Ω^- particle with quark content *sss* and spin-parity $J^P = \frac{3}{2}^+$. This particle was significant in being made of three strange quarks and was discovered at Brookhaven in 1964, where figure 56 shows the original bubble chamber event.

- **Spatial**: The parity is positive: $P = (-1)^{L=0} = +1$ implying a symmetric spatial state with respect to exchange of labels.
- **Flavour**: The flavour state is $|s\rangle_1|s\rangle_2|s\rangle_3$ for quarks labelled 1,2,3 and is symmetric.
- **Spin**: With no orbital angular momentum $L = 0$, the only way to obtain $J = \frac{3}{2}$ is to have all the quarks' spins aligned $|\uparrow\rangle_1|\uparrow\rangle_2|\uparrow\rangle_3$, which is symmetric.

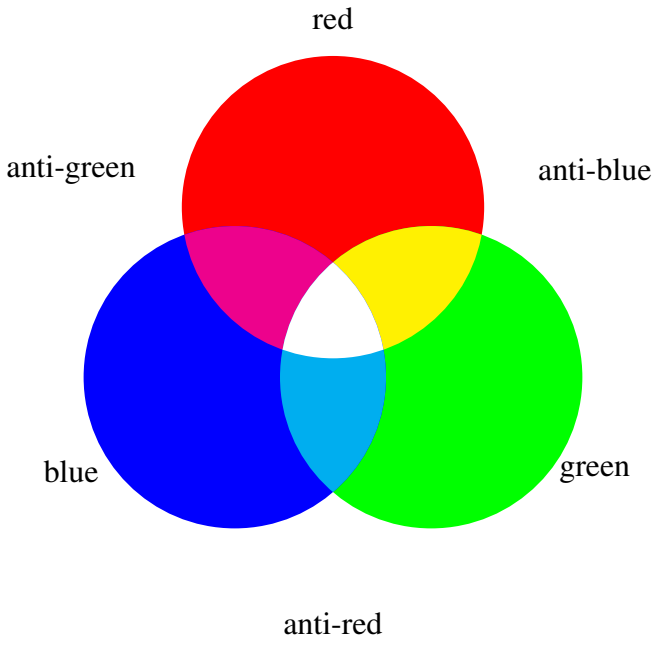

Figure 57: **Mnemonic for colour charge addition**. Analogy with colour theory for the addition of charge associated with the strong force.

- **Colour**: The space-flavour-spin combined wavefunction is symmetric. As baryons are fermions, they must be antisymmetric with respect to exchange of labels. By introducing a new degree of freedom for quarks, we can satisfy this condition. We call this **colour** because it is a helpful analogy to the fact only colour-neutral states are experimentally observed. We can define the colour wavefunction to be manifestly antisymmetric via a 3×3 determinant (normalised by $1/\sqrt{6}$):

$$|\psi_{\text{colour}}\rangle = \frac{1}{\sqrt{6}} \begin{vmatrix} r_1 & g_1 & b_1 \\ r_2 & g_2 & b_2 \\ r_3 & g_3 & b_3 \end{vmatrix} \tag{9.10}$$

  This determinant flips sign if we exchange the labels on any two rows, satisfying antisymmetry with respect to label exchange.

The analogy of colour charge with the additive colour theory of light. This combination of three colours is colour-neutral:

$$\text{red} + \text{green} + \text{blue} = \text{neutral}. \tag{9.11}$$

But this combination of colour and anticolour is also colour-neutral:

$$\text{blue} + \text{anti-blue} = \text{neutral}. \tag{9.12}$$

Equating the two neutral states, we can therefore conclude that

$$\text{red} + \text{green} = \text{anti-blue}. \tag{9.13}$$

Interestingly, this works analogously to the additive colours of light of adding red and green light to make yellow, and the 'opposite of yellow' is indeed blue (figure 57).

While these colours are not how hadrons literally look, this certainly serves as a useful memory aid. Finally, colour is related to the **confinement hypothesis**:

> Confinement hypothesis: coloured objects cannot exist in isolation.

This provides an initial phenomenological rule for why free quarks are not observed in nature and instead confined within colourless hadrons. Given this, how we can ever hope to experimentally test the existence of quarks?

The idea that quarks are elementary particles initially proved controversial as nothing more than mere mathematical constructs. Explaining the particle zoo via symmetry arguments was theoretically appealing but the existence of quarks was unclear. This mirrors how the reality of atoms remained inconclusive throughout the nineteenth century, yet was a helpful construct to explain the observed law of multiple proportions. Fractional electric charges certainly sounded outlandish. Quark scepticism endured for many years, yielding eloquent quotations[51] by Murray Gell-Mann (c. 1966):

> "The idea that mesons and baryons are made primarily of quarks and gluons is hard to believe."

and James Bjorken (c. 1967):

> "Additional data are necessary and very welcome to destroy the picture of elementary constituents."

As we shall now see, a landmark series of experiments firmly establish the existence and properties of quarks and colour.

[51] https://indico.cern.ch/event/147420/contributions/1384964

10 Revealing nuclear substructure

This section explores the empirical evidence addressing these questions:

- How do we know protons and neutrons are not point-like?
- How do we measure the size and shape of protons and nuclei?
- How do we show there are point-like substructure inside protons?
- How do we acquire evidence for the existence of quarks?
- How do we know quarks are spin-half fermions and have fractional charge?

Gathering evidence for these questions required ambitious high-energy scattering experiments. Figure 58 shows schematically the process of probing the proton and its structure from low to higher energies. This parallels the process of the Manchester experiments discovering the atomic nucleus.

Fortuitously in 1961, US Congress approved construction of a two-mile long accelerator at Stanford Linear Accelerator Center, California devised in the prior decade. The landmark experiments spearheaded by Jerome Friedman, Henry Kendall, and Richard Taylor began in 1966. Increasing energies of accelerators enabled measuring the finite size and eventually substructure of the proton precisely, firmly establish the existence and dynamics of quarks.

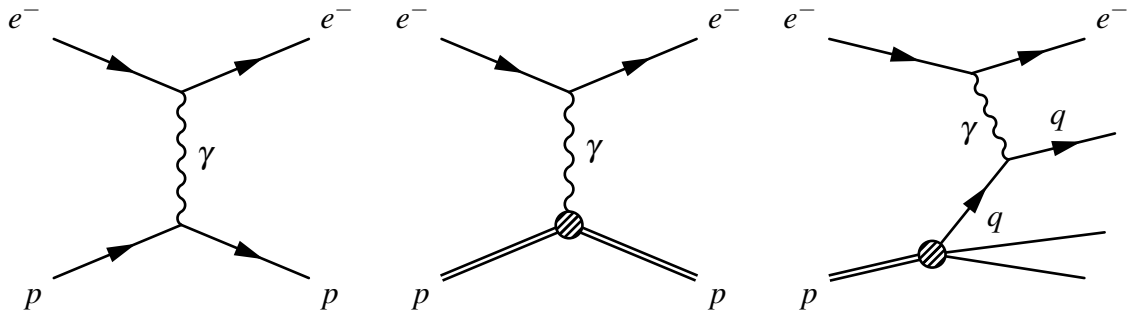

(a) **Low energy**
$\lambda_e \gg r_p$: point-like proton

(b) **Medium energy**
$\lambda_e \sim r_p$: finite-sized proton

(c) **High energy**
$\lambda_e \ll r_p$: quarks in proton

Figure 58: **Electron–proton scattering at increasingly high energies**. At low energies, the electron wavelength λ_e is sufficiently large to interact with the proton as a point-like particle. At a critical wavelength $\lambda_e \sim r_p$ where the electron wavelength and proton size is comparable, the finite size effects become detectable. At higher energies with electron wavelength much smaller than the proton size $\lambda_e \ll r_p$, the electrons scatter off the internal substructure, namely quarks.

This eventually led to the discovery of the charmonium as bound states of charm quarks. These experiments form the precursor to quantum chromodynamics.

10.1 Nuclear form factors

The central idea of nuclear scattering parallels Geiger–Marsden–Rutherford scattering five decades earlier revealing the existence of the proton as atom substructure. We bombard a target with sufficiently high energy particles i.e. with de Broglie wavelengths reach the order of magnitude of the target's size. This allows us to resolve any substructure in the target characterised by a **form factor**.

Rutherford scattering probed atoms to reveal the nucleus and later deep inelastic scattering probed nuclei to reveal quark substructure.

Scattering as Fourier transform We can define the spatial distribution of the nuclear charge density $\rho(\mathbf{r})$ to be[52]

$$\int \rho(\mathbf{r})\,\mathrm{d}^3\mathbf{r} = Ze. \tag{10.1}$$

The potential energy for a particle of charge ze with coordinate $\mathbf{r}$ incident on the target nucleus of charge Z is then ($\hbar = c = \varepsilon_0 = 1$)

$$V(\mathbf{r}) = \frac{ze}{4\pi}\int \frac{\rho(\mathbf{r}')}{|\mathbf{r}-\mathbf{r}'|}\mathrm{d}^3\mathbf{r}'. \tag{10.2}$$

where $\mathbf{r}'$ is the coordinate from the origin to a charge element of the nucleus. Applying the Born approximation (weak potential i.e. nucleus does not recoil), the scattering amplitude $\langle\mathbf{k}'|V|\mathbf{k}\rangle$ is the Fourier transform of this potential (equation (4.23))

$$\langle\mathbf{k}'|V|\mathbf{k}\rangle = \frac{1}{(2\pi)^3}\int \mathrm{d}^3\mathbf{r}\,\mathrm{e}^{\mathrm{i}\mathbf{q}\cdot\mathbf{r}}\left[\frac{ze}{4\pi}\int\frac{\rho(\mathbf{r}')}{|\mathbf{r}-\mathbf{r}'|}\mathrm{d}^3\mathbf{r}'\right]. \tag{10.3}$$

Substituting $\mathbf{R} = \mathbf{r} - \mathbf{r}'$, holding $\mathbf{r}'$ fixed so that $\mathrm{d}^3\mathbf{R} = \mathrm{d}^3\mathbf{r}$, we obtain

$$\langle\mathbf{k}'|V|\mathbf{k}\rangle = \underbrace{\frac{Zze^2}{4\pi}\frac{1}{(2\pi)^3}\int\frac{\mathrm{e}^{\mathrm{i}\mathbf{q}\cdot\mathbf{R}}}{|\mathbf{R}|}\mathrm{d}^3\mathbf{R}}_{\text{Point-like}}\underbrace{\left[\frac{1}{Ze}\int\mathrm{d}^3\mathbf{r}'\,\rho(\mathbf{r}')\mathrm{e}^{\mathrm{i}\mathbf{q}\cdot\mathbf{r}'}\right]}_{\text{Form factor } F(\mathbf{q})}. \tag{10.4}$$

We define the **nuclear form factor**

$$\boxed{F(\mathbf{q}) \equiv \frac{1}{Ze}\int\rho(\mathbf{r}')\,\mathrm{e}^{\mathrm{i}\mathbf{q}\cdot\mathbf{r}'}\mathrm{d}^3\mathbf{r}'} \tag{10.5}$$

[52] Some texts describe the nuclear charge distribution as given by $Ze\rho(\mathbf{r})$ such that $\int\rho(\mathbf{r})\mathrm{d}^3\mathbf{r} = 1$. Our definition has the factor of Ze effectively absorbed into $\rho(\mathbf{r})$.

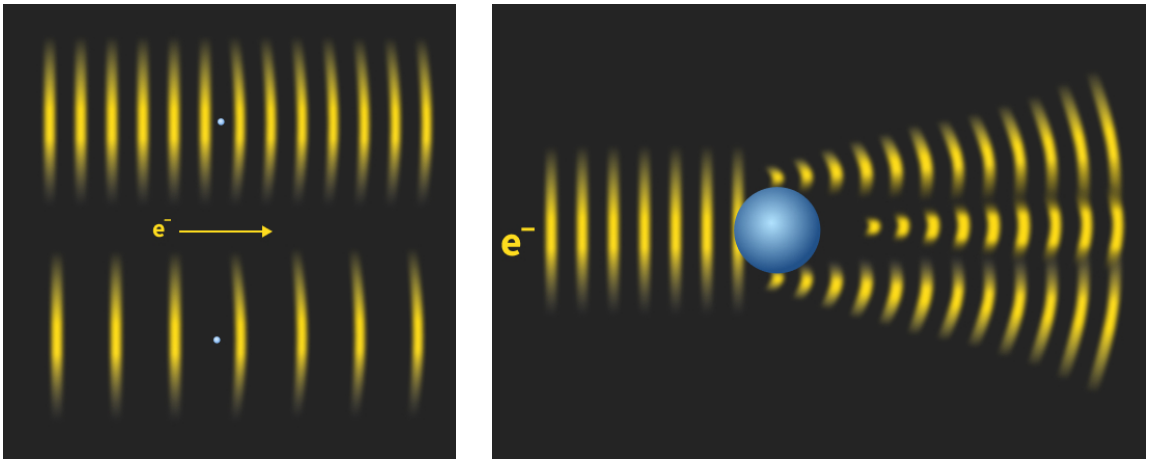

(a) Point-like target (b) Finite-size target

Figure 59: **My impressionistic cartoon of electron waves scattering off targets**. This is displayed in real space, showing the electron as yellow plane waves and target as a blue sphere. When the target is a point-like object (e.g. quarks or insufficient energy to resolve proton size), the electron waves respond identically for high (upper) and low (lower) frequencies as there is no intrinsic scale. When the electron wavelengths are comparable to the proton size, a non-trivial scattering pattern appears, which is the Fourier transform of the target spatial distribution.

Crucially, the measurable differential cross-section is

$$\frac{\mathrm{d}\sigma}{\mathrm{d}\Omega} = |F(\mathbf{q})|^2 \left(\frac{\mathrm{d}\sigma}{\mathrm{d}\Omega}\right)_{\text{Point-like}} . \tag{10.6}$$

The form factor is a simple multiplicative modification of the point-like differential cross-section when measuring in momentum transfer space $\mathbf{q}$. In scattering experiments, we can therefore measure the form factor $F(\mathbf{q})$ and inverse Fourier transform to obtain the spatial charge distribution of the target. Fourier transforming a charge distribution is of course not confined to nuclear scattering physics, but indeed all of quantum scattering with matter waves. This also applies to X-ray crystallography and neutron scattering to decipher the spatial structure of wide-ranging materials from crystals lattices to DNA.

To illustrate these concepts, figure 58 shows the physical picture of probing the nucleus with increasingly high energy electron waves. This shows the historical progress in understanding protons from point-like particle, to determination of its finite size, and finally proton substructure that laid the foundations for quarks. If electron with energies $< 1\,\mathrm{GeV}$ collide with nucleons, the interactions are dominated by elastic scattering. As we increase this en-

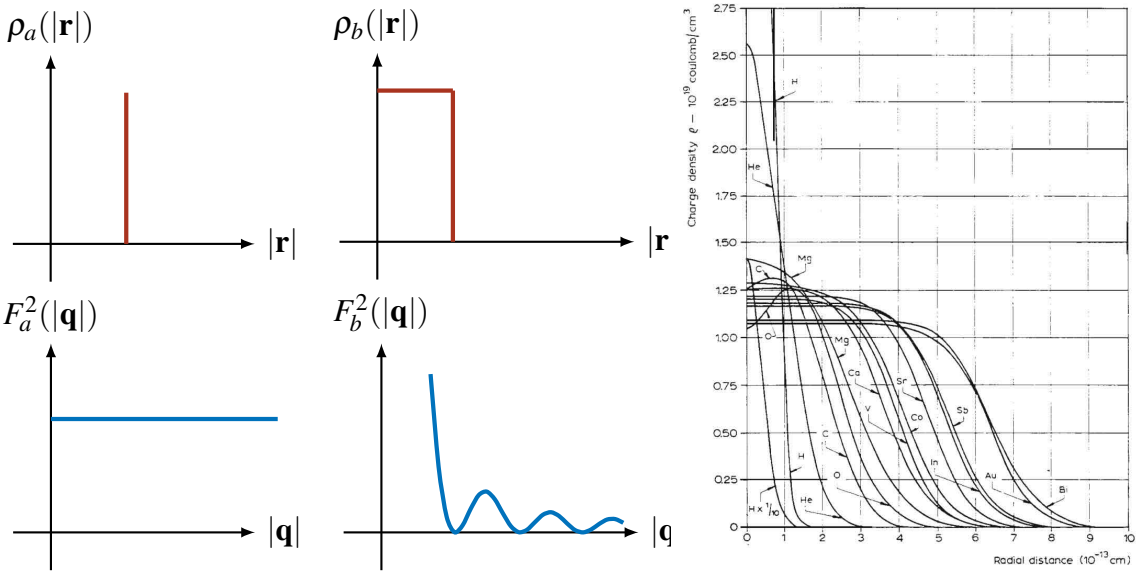

(a) Point-like $\rho(r)$ (b) Hard sphere $\rho(r)$ (c) Nuclear charge densities

Figure 60: **Charge spatial distributions and their Fourier transform**. Distributions $\rho(|\mathbf{r}|)$ (upper) and the corresponding form factor $F(|\mathbf{q}|)$ corresponding to their Fourier transform (lower). Displayed examples are the point-like and hard sphere models of the nucleus. The plot summarises various nuclear charge densities determined in the 1950s from electron scattering experiments; figure from Hofstadter Nobel lecture (1961), Ref. [64].

ergy > 1 GeV, the elastic scattering cross-section decreases dramatically. Elastic scattering of electron-proton interactions models the proton as a point-like particle that stays intact

$$e^- + p \to e^- + p. \tag{10.7}$$

At higher energies, it became clear the proton had a finite size due to its measured form factor.

Point-like proton: Mott scattering

At low energies where the probe electron wavelength was much larger than the proton size $\lambda_e \ll \lambda_p$, the electron effectively interacts with the proton as a point-like particle. As there is no physical scale to the target, the electron has the same scattering behaviour for all incident energies. This effective scale invariance of the scattering is sketched in figure 59a, where outgoing waves are the same in both energies. Mathematically, this is reflected in the Fourier transform shown in figure 60a.

We can model the nucleus as a point charge at the origin using a delta function

$$\rho_1(\mathbf{r}') = Ze\delta^{(3)}(\mathbf{r}') \tag{10.8}$$

Applying (10.5), the form factor is the Fourier transform of a delta function at the origin which evaluates to unity

$$F_1(|\mathbf{q}|) \equiv \frac{1}{Ze}\int Ze\delta^{(3)}(\mathbf{r}')\, \mathrm{e}^{\mathrm{i}\mathbf{q}\cdot\mathbf{r}'}\mathrm{d}^3\mathbf{r}' = 1 \tag{10.9}$$

A point-like charge distribution is modelled as a delta function $\rho(\mathbf{r}) = Qe\delta(\mathbf{r})$, so the form factor $F(\mathbf{q})$ is constant versus the probe momentum transfer $|\mathbf{q}|^2$. This is equivalent to Rutherford scattering ${}^4_2\alpha\, p \to {}^4_2\,\alpha p$.

Relativistic electrons with initial energy E_i scattering off a proton with negligible recoil $m_e \ll E_i \ll m_p$ is known as **Mott scattering** $e^- p \to e^- p$. The cross-section is given by (see Thomson chapter 7)

$$\left(\frac{\mathrm{d}\sigma}{\mathrm{d}\Omega}\right)_{\text{Mott}} = \left[\left(\frac{e^2}{4\pi}\right)^2 \frac{1}{4E_i^2\sin^4(\theta/2)}\right]\cos^2\frac{\theta}{2}. \tag{10.10}$$

The part in square brackets has the familiar form of the Rutherford scattering cross-section.

Finite-size proton As the electron energy increases to become comparable to the proton size $\lambda_e \sim r_p$, the finite size. This is the next-to-minimal model, where we can model the nucleus as a hard sphere of radius a with a spherically symmetric uniform charge density of ρ_0:

$$\rho_2(r') = \begin{cases} \rho_0 & r' \le a \\ 0 & r' > a \end{cases} \tag{10.11}$$

Evaluating the angular dependence, the form factor for a generally spherically symmetric charge distribution $\rho(\mathbf{r}') = \rho(r')$ is

$$F_2(|\mathbf{q}|) = \frac{4\pi}{Ze|\mathbf{q}|}\int_0^\infty r'\rho(r')\sin\left(r'|\mathbf{q}|\right)\mathrm{d}r' \tag{10.12}$$

Using (10.11), we obtain

$$F(|\mathbf{q}|) = \frac{3}{\beta^3}[\sin(\beta) - \beta\cos(\beta)], \quad \text{where} \quad \beta \equiv a|\mathbf{q}|. \tag{10.13}$$

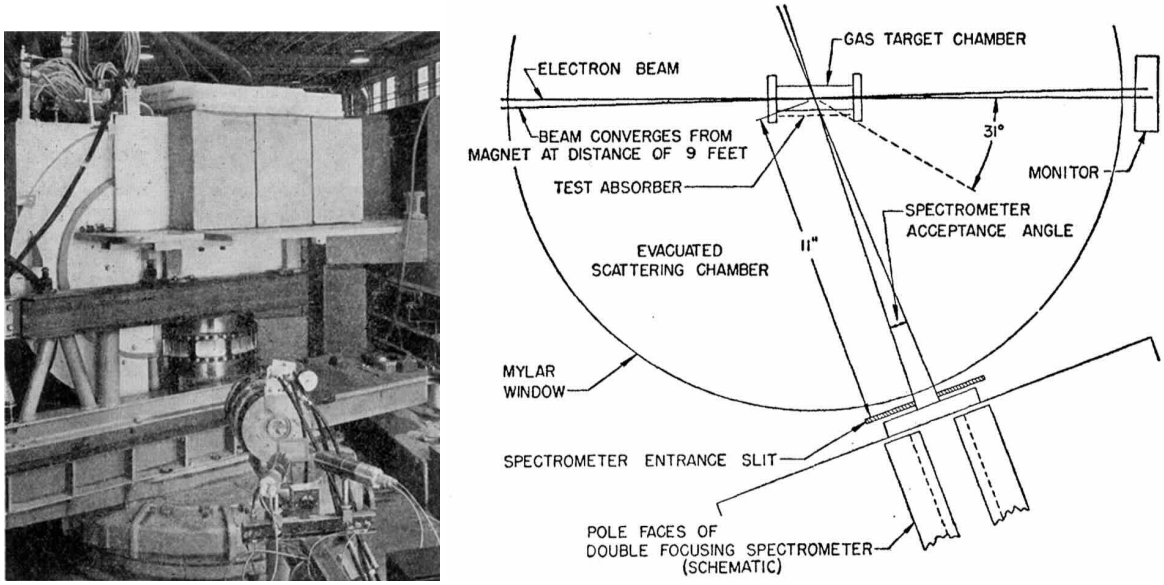

(a) Spectrometer photo

(b) Target chamber schematic [65]

Figure 61: **Apparatus of 190 MeV Stanford electron scattering experiment in 1954**. In the photo, the spectrometer is the larger semi-circular device on the left of the photo with the rectangular blocks to its right comprising the lead/paraffin shielding, with the thin target windows surrounding the scattering chamber just below these. Figures from Ref. [64].

This form factor is sketched heuristically in figure 59b and the exact Fourier transform is plotted in figure 60b. The physical picture is that the finite-size sphere induces an modulated scattering pattern, set by a concrete scale a, namely the size of the sphere. This looks uncannily similar to what we learn in wave optics diffraction pattern through a single slit $\propto \sin(ka)/(ka)$. Of course, this is not completely unexpected given light and matter are both waves.

Stanford electron scattering experiments

In 1954 at Stanford, Robert Hofstadter and Robert McAllister speared landmark experiments using electron beams up to 190 MeV scatter off nuclei (figure 62). Hofstadter notes in his Nobel lecture[53] how Eva Wiener designed the high-pressure, thin-wall gas chambers crucial for housing hydrogen targets but did not live to see the remarkable scientific results of her apparatus.

[53] https://www.nobelprize.org/uploads/2018/06/hofstadter-lecture.pdf

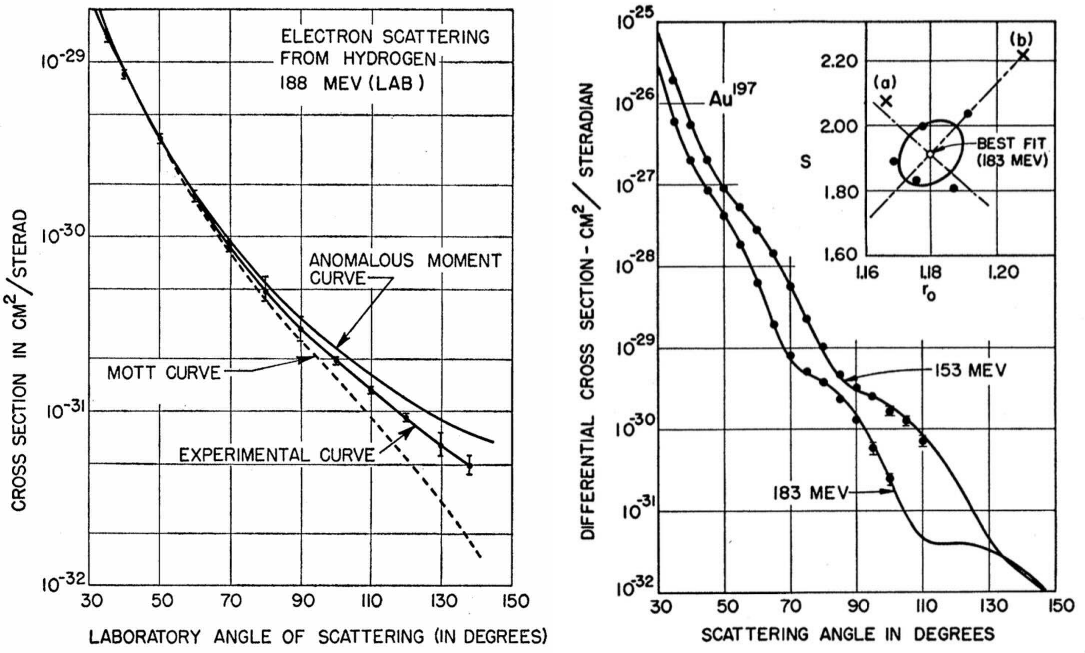

(a) Electron–proton scattering [66] (b) Electron–gold scattering [65]

Figure 62: **Results of electron scattering off proton and gold**. Electron–proton and electron–nucleus scattering experiments performed at Stanford in 1955–56. .

The electron scattering results revealed that the proton has finite size rather than being point-like with a magnetic moment as electrons do (figure 62a). Fits to the data determined to proton to have an exponential charge distribution $\sim \exp\left(-r^2/R^2\right)$ with a root-mean-square radius of around 0.8×10^{-15} m [66].

Using the nuclear form factors calculated by theorists Donald Yennie and colleagues [67], this enabled detailed characterisation of nuclei. Figure 62b shows one of these scattering patterns, with the characteristic $\sim \sin(x)/(x)$ modulation of a quasi-hard sphere. These series of landmark experiments are lucidly reviewed in Ref. [64].

Following these experiments were precise determination of nuclear form factors up to 900 MeV electron energies up to what was called "Mark III". However, pushing beyond 1 GeV required far greater resources. Meeting with Wolfgang Panosfky in 1956, Hofstadter lobbied for an order of magnitude increase in electron energies to be built at Stanford, a proposal known affectionately as "Project M" for Monster[54]. A detailed proposal was drawn up in 1957 for a two-mile accelerator, what was to become the Stanford Linear Accelerator

[54] https://www.slac.stanford.edu/vault/pubvault/ST14no3_Panofsky.pdf

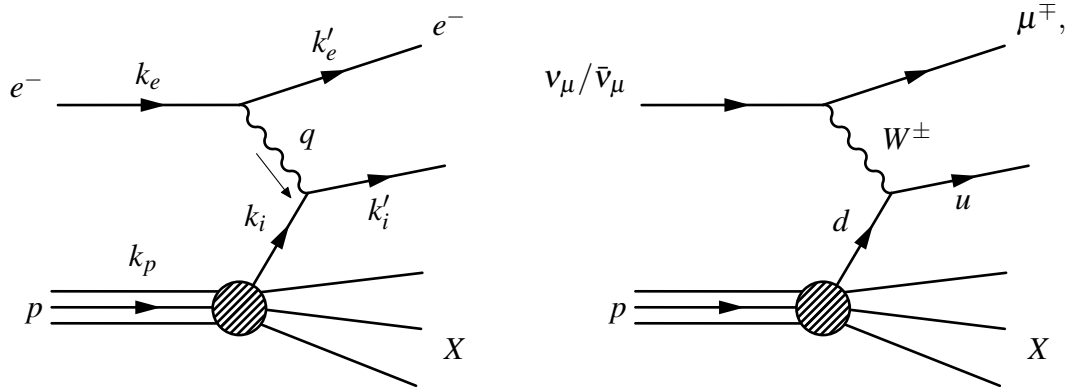

(a) Electron–quark with momentum labels

(b) Neutrino deep inelastic scattering

Figure 63: **Deep inelastic scattering (DIS) diagrams**. An electron e^- strikes the proton p, with the following momentum labels. We measure the outgoing k'_e relative to initial k_e electron with $q = k_e - k'_e$ momentum transferred to the probe photon. The photon scatters off internal substructure (a quark) inside the proton (labelled i), which has initial k_i and outgoing k'_i momentum. The initial proton momentum is k_p, while the remnants of the proton breakup is denoted X. On the right, the analogous diagram with neutrino DIS via a charged current interaction mediated by a $W^\pm$ boson.

Center. Congress approved funding in 1961 and construction started in 1962. This set the stage for deep inelastic scattering to look inside the proton.

10.2 Deep inelastic scattering

Ramping up the incident electron energies to well over a GeV enables it to scatter off much smaller scales than the size of the proton. This contrasts with elastic scattering where the outgoing proton stays intact $e^- p \to e^- p$. Deep inelastic scattering instead probes inside the proton and results in the outgoing proton breaking up into a hadron system X:

$$e^- + p \to e^- + (p \to X). \tag{10.14}$$

Deep inelastic scattering (figure 63) provides direct evidence for substructure, namely quarks in nucleons. The electron interacts with the internal substructure, namely a quark, via a photon mediating the electromagnetic interaction.

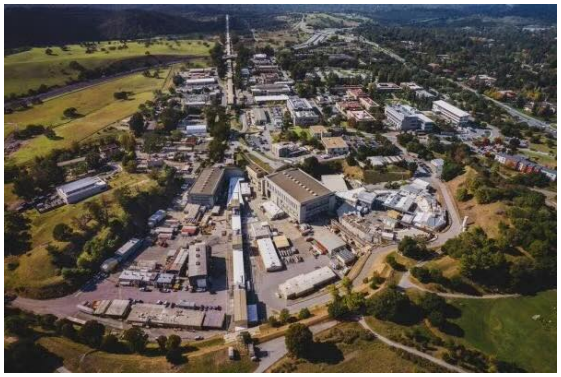

(a) SLAC aerial view

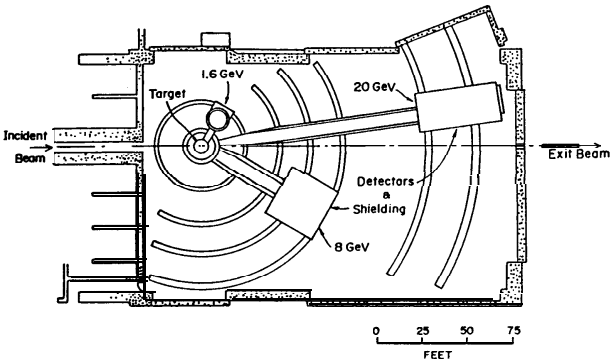

(b) End station A plan view

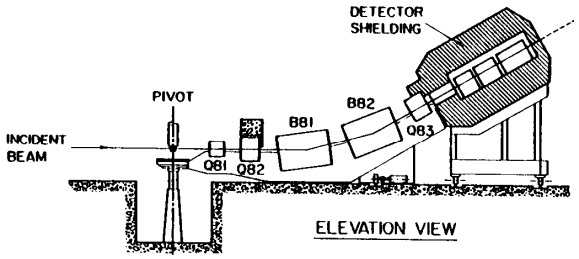

(c) 8 Gev arm elevation view

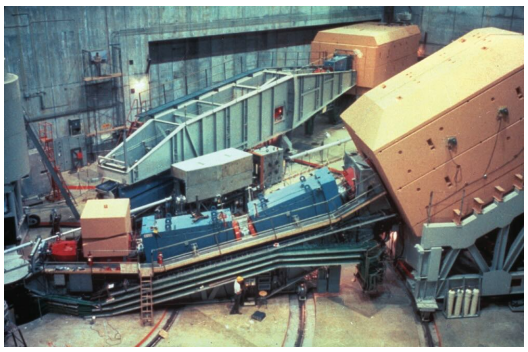

(d) Photo of 8 GeV spectrometer

Figure 64: **Apparatus of MIT–SLAC deep inelastic scattering experiments**. Electrons are accelerated by a two-mile long beam line up to 20 GeV. This strikes a hydrogen target and magnetic spectrometers measure the scattered electron energy loss relative to the incident energy $\nu = E - E'$. These can be rotated to measure the scattered electron at various angles relative to the beamline $\theta_{ee'}$. Figures from SLAC National Accelerator Laboratory, 1990 Kendall Nobel prize lecture and R. Muffley/SLAC/APS.

For the kinematics of figure 63, we use k to denote the four-momenta (to save confusion with p for proton)

$$k_e = \begin{pmatrix} E_e \\ \mathbf{k}_e \end{pmatrix}, \quad k'_e = \begin{pmatrix} E'_e \\ \mathbf{k}'_e \end{pmatrix}, \quad k_p = \begin{pmatrix} M_p \\ \mathbf{0} \end{pmatrix}. \tag{10.15}$$

We define the momentum transferred q to the photon in terms of initial and outgoing electron

$$q = k_e - k'_e = \begin{pmatrix} E_e - E'_e \\ \mathbf{q} \end{pmatrix}. \tag{10.16}$$

Conserving momentum at the photon–internal-structure vertex $k_i' = k_i + q$ then squaring gives

$$(k_i')^2 = q^2 + k_i^2 + 2k_i \cdot q. \tag{10.17}$$

Neglecting the mass of the internal substructure $k_i^2 = k_i'^2 \approx 0$ gives

$$2k_i \cdot q = -q^2. \tag{10.18}$$

The internal substructure carries a fraction x of the proton momentum $k_i = xk_p$ and working in the proton rest frame gives:

$$x = \frac{-q^2}{k_p \cdot q} = \frac{-q^2}{2(E_e - E_e')M_p}. \tag{10.19}$$

Following notation of most textbooks and historical papers[55], we define $Q^2 = -q^2$ and $\nu = E_e - E_e'$ to yield the Bjorken-x formula:

$$x = \frac{Q^2}{2\nu M_p}. \tag{10.20}$$

Another useful observable is the inelasticity y, which corresponds to the fractional energy lost by the electron

$$y = 1 - \frac{E_e'}{E_e} = \frac{\nu}{E_e}. \tag{10.21}$$

This arises from the Lorentz invariant quantity $y = (k_p \cdot q)/(k_p \cdot k_e)$ evaluated in the proton rest frame.

Conserving momentum at the electron–photon vertex $q = k_e - k_e'$ and squaring, we find

$$\begin{aligned} q^2 &= (k_e - k_e')^2 && (10.22)\\ &= k_e^2 + k_e'^2 - 2k_e \cdot k_e' && (10.23)\\ &= 2m_e^2 - 2(E_e E_e' - \mathbf{k}_e \cdot \mathbf{k}_e') && (10.24) \end{aligned}$$

In the ultra-relativistic limit $m_e \to 0$, this simplifies down to

$$Q^2 = -q^2 = 2E_e E_e'(1 - \cos\theta_{ee'}). \tag{10.25}$$

[55] The literature can cause nightmares by flip-flopping between uppercase and lowercase q, Q to denote momentum transfer $q^2 = \pm(k - k')^2$, quark charge $q = \frac{1}{3}e, \frac{2}{3}e, \ldots$, and quark flavour $q = u, d, s \ldots$. Sometimes p, P interchanges between proton and momentum, rendering proton momentum P_p. My past futile attempts for disambiguation denoted four-vectors by sans-serif Q or electric charge by calligraphic $\mathscr{Q}$ script, but these are difficult to distinguish in handwriting. Like linguistic ambiguity, e.g. *lead* can denote directing a team or the chemical element with 82 protons, context usually brings clarity. Apologies to notational purists.

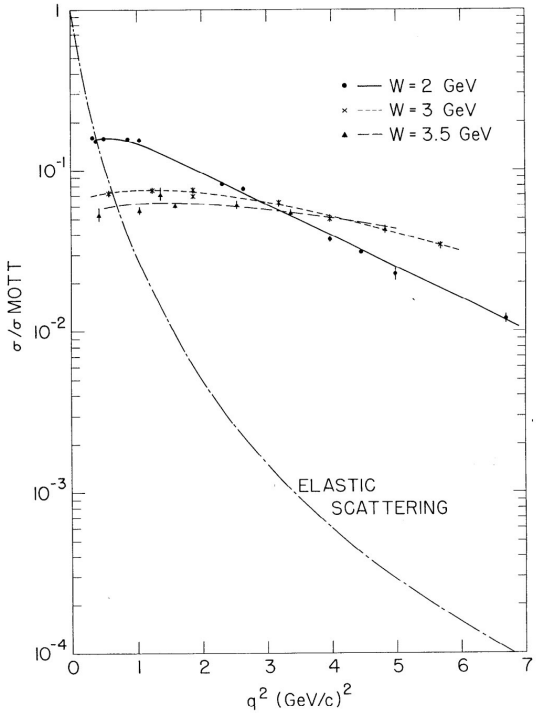

(a) Cross-sections vs q^2

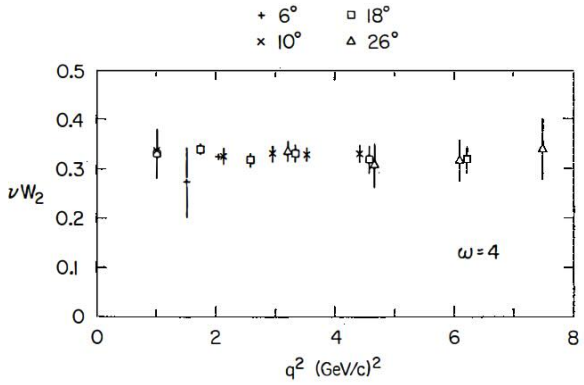

(b) Scaling vs q^2

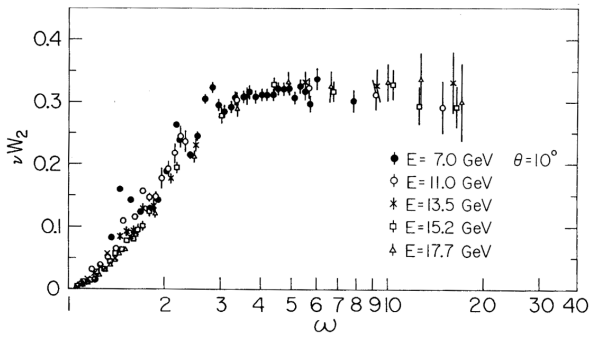

(c) Scaling vs $\omega = 1/x$

Figure 65: **Deep inelastic scattering data**. This supports the hypothesis of electron scattering off point-like internal substructure of the proton. Note how the product of the proton structure function (historical notation W_2) with $\nu = E_e - E'_e$ is nearly independent of q^2 for $x = 1/\omega = 1/4$, exhibiting scale invariance. Figures from Refs. [68, 69].

Finally, the invariant mass W of the system of hadrons comprising the fragmented proton X is inferred by momentum conservation

$$W_X = (k_p + q)^2. \tag{10.26}$$

Given we know the incoming electron beam energy E_e, we only need to measure two observables to determine Q^2 and ν: the outgoing scattered electron energy E'_e and scattered angle relative to the incident $\theta_{ee'} = \theta'_e - \theta_e$.

The MIT and SLAC groups performed such landmark experiments in the late 1960s, accelerating electrons between 5 and 20 GeV onto a liquid hydrogen target. The historical experimental apparatus for this is shown in figure 64.

In the deep inelastic regime where $Q^2 \gg m_p^2 y^2$, the Lorentz invariant differential cross-

section for a single photon exchange in terms of Q, x, y is given by (see Thomson Chapter 8):

$$\frac{\mathrm{d}^2\sigma}{\mathrm{d}Q\,\mathrm{d}x} = \frac{4\pi\alpha^2 s}{Q^4}\left[y^2 F_1(x,Q^2) + \frac{(1-y)}{x}F_2(x,Q^2)\right]. \tag{10.27}$$

The objects $F_1(x,Q^2), F_2(x,Q^2)$ are called structure functions. In the elastic case, F_1 corresponds to the purely magnetic interaction while F_2 has electric and magnetic contributions. To experimentally determine this, we measure the event rates as a function of the observables Q, x, y. We can first count events holding x fixed and scanning y by varying the incident electron energy E_e. We then use these measurements of how $\mathrm{d}^2\sigma/(\mathrm{d}Q\,\mathrm{d}x)$ varies with y to disentangle the relative sizes of the two structure functions. In modern statistical analysis, this corresponds to a simultaneous differential fit of the Q, x, y variables to extract F_1, F_2.

Figure 65 shows the initial data [68]. The suppression of the elastic cross-section at high Q^2 is not observed. This suppression arises from the so-called Rosenbluth formula, which extends the Mott cross-section to include the electric G_E and magnetic G_M dipoles of the proton (see Thomson chapter 7)

$$\frac{\mathrm{d}\sigma}{\mathrm{d}\Omega} = \left[\frac{G_E^2 + cG_M^2}{1+c} + 2cG_M^2\tan^2\frac{\theta}{2}\right]\frac{E_e'}{E_e}\left(\frac{\mathrm{d}\sigma}{\mathrm{d}\Omega}\right)_{\text{Mott}}, \tag{10.28}$$

where $c = Q^2/4m_p^2$. The magnetic dipole has the empirically determined form $G_M^2 \propto (1 + Q^2/0.71\ \text{GeV}^2)^{-2}$ and dominates in the high Q^2 limit, giving a fast suppression to the elastic cross-section

$$\left(\frac{\mathrm{d}\sigma}{\mathrm{d}\Omega}\right)_{\text{elastic}} \propto \frac{1}{Q^6}\left(\frac{\mathrm{d}\sigma}{\mathrm{d}\Omega}\right)_{\text{Mott}}. \tag{10.29}$$

Instead the much broader spectrum is observed showing inelastic scattering. The inelastic cross-section for production of hadrons remains relatively constant and begins to dominate at high energies.

For low x (high $\omega = 1/x$) values, there is the same characteristic **scale invariance** for different beam energies. This is sometimes called Bjorken scaling. The physical interpretation of this observed arises from the electrons probing targets that lack any size or scale, i.e. there are point-like objects inside the proton.

The electron de Broglie wavelength becomes small enough to scatter incoherently off the any point-like entities within the nucleon. Historically these were called **partons** when quark theory remained controversial. By measuring the kinematic properties of the scattered electron, we can deduce properties regarding the nucleon substructure. We observe the scattered quarks as hadrons, mainly mesons, due to confinement.

10.3 Evidence for quark properties

We now discuss the empirical evidence for quark properties easily taken for granted and even trivialised as "historical". The conundrum is that quarks are confined inside protons and neutrons by colour confinement. These objects that seem to be unobservable, by construction. So how is it possible to empirically study their properties such as spin, charge, and flavour composition? This is where ingenuous phenomenological arguments and experimental data are needed.

Evidence for spin-half. Electrons scattering off a distinct spin-half point-like charged particle such as a muon is given by (section 9 of Ref. [1])

$$\frac{\mathrm{d}^2\sigma}{\mathrm{d}Q\,\mathrm{d}x} = \frac{2\pi\alpha^2 s}{Q^4}\left[1+(1-y)^2\right]. \tag{10.30}$$

To consider electron–quark scattering inside a nucleon, we consider the fact quarks have fractional charge labelled q_i for flavour i, so we replace $\alpha \to \alpha\sum_i q_i^2$ and they carry x_i momentum fraction so we replace $s \to x f_i(x) s$, where $f_i(x)$ is the probability distribution of quark i. The resulting differential cross-section is then

$$\frac{\mathrm{d}^2\sigma}{\mathrm{d}Q\,\mathrm{d}x} = \frac{4\pi\alpha^2 s}{Q^4}\sum_i q_i^2 x f_i(x)\left[(1-y)+\frac{1}{2}y^2\right]. \tag{10.31}$$

By assuming electrons scatter off effectively free spin-half point-like fermions with fraction charge, this fixes the coefficients prefixing $(1-y)$ and y^2. Equating these coefficients with the phenomenological differential equation (10.27) that link to observables gives

$$2xF_1(x) = F_2(x). \tag{10.32}$$

This central result is the **Callan–Gross relation** by Curtis Callan and David Gross in 1969 [70]. Scattering off a spin-0 particle would result in $F_1(x) = 0$. Historically, the SLAC experiments measured this quantity to test the different spin predictions of the quark–parton model:

$$\frac{2xF_1(x)}{F_2(x)} = \begin{cases} 0 & \text{spin-0 quarks,} \\ 1 & \text{spin-1/2 quarks.} \end{cases} \tag{10.33}$$

Figure 66 displays the experimental data from SLAC, providing evidence for the spin-1/2 nature of quarks and disfavouring spin-0.

The quark–parton model also constrains

$$F_2(x,Q^2) = \sum_i q_i^2 x f_i(x). \tag{10.34}$$

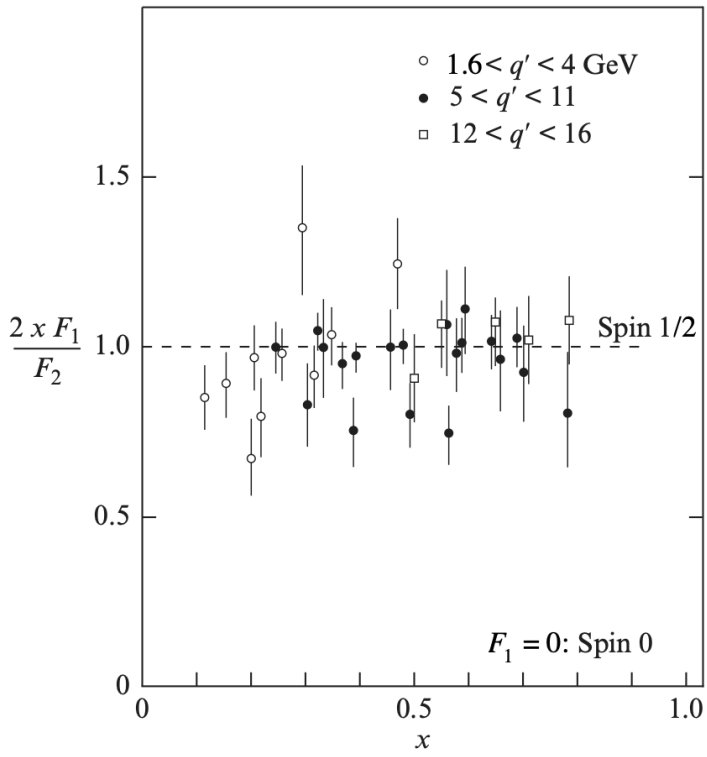

Figure 66: Data testing the Callan–Gross relation (10.33), favouring quarks being spin-1/2 rather than spin-0 particles. Adapted from Ref. [1].

This extends the Bjorken-x scaling to show that F_2 only depends on x and not Q^2.

Evidence for fractional charge: In 1972, the muon-neutrino beam created by the Proton Synchrotron at CERN is directed at the Gargemelle bubble chamber (figure 67).

Figure 63b shows the neutrino–quark scattering via a $W^{\pm}$ boson, a charged-current interaction before the discovery of the $W^{\pm}$. We can measure this process and compare this against the SLAC data for electron–quark scattering. Neglecting strange quarks, the key results are comparing electron–nucleon scattering with neutrino–nucleon:

$$\frac{\frac{1}{2}\int \mathrm{d}x\,\left[F_2^{ep}(x)+F_2^{en}(x)\right]}{\frac{1}{2}\int \mathrm{d}x\,\left[F_2^{\nu p}(x)+F_2^{\nu n}(x)\right]} = \frac{Q_u^2+Q_d^2}{2} = \frac{5}{18} = \frac{1}{3.6}. \tag{10.35}$$

Figure 68 shows the data supporting this, which firmly establish the fractional charge of quarks [71].

Evidence for 3 valence quarks: The Gross–Llewellyn-Smith (GLS) sum rule provides

Figure 67: Gargamelle detector now on display at the CERN park for visitors. Image: CERN

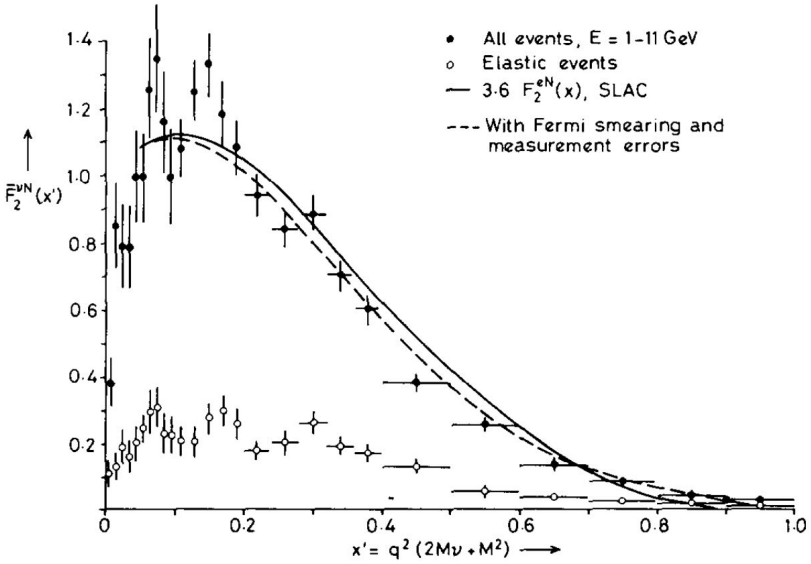

Figure 68: Combined SLAC–Gargamelle data [71] supporting the fractional charges of quarks. The black points are the neutrino-quark data, compared to the lines based on the electron-quark data scaled by $2/(Q_u^2 + Q_d^2) = 18/5 = 3.6$.

evidence for the number of valence quarks in a proton and neutron:

$$\int F_3^{\nu n}(x) = \int [u_v(x) + d_v(x)]\mathrm{d}x = N_q^{\text{valence}} - N_{\bar{q}}^{\text{valence}} = 3.2 \pm 0.6. \tag{10.36}$$

The actual value is closer to 2.5, with the remainder arising from the gluons.

Evidence for gluon: Finally, the total momentum carried by the quark content of a nucleon N and should equal unity:

$$S_q^{\text{theory}} = \int_0^1 \mathrm{d}x F_2^{\nu N}(x) = \int_0^1 \mathrm{d}x x \left[u(x) + \bar{u}(x) + d(x) + \bar{d}(x) + s(x) + \bar{s}(x)\right] = 1. \quad (10.37)$$

However, Gargemelle measures this to be half the expected value to be

$$S_q^{\text{experiment}} = \int_0^1 \mathrm{d}x F_2^{\nu N}(x) = 0.49 \pm 0.07. \quad (10.38)$$

This implies that half the momentum of the proton is carried by its constituents do not couple to the electroweak interactions. What else is inhabiting the proton? This is of course the first indication for the existence of particles that only interact via the strong force: the gluon.

10.4 Charmonium

Before turning to the gluon, which completes the picture for quantum chromodynamics, we recount a key discovery that coincided with the acceptance of the quark–parton model. This is the charmonium, comprising a bound state of charm and anti-charm quarks. Advances in accelerator technology in the late 1960s and 70s were needed to discover heavier quarks.

The J/ψ state was discovered in 1974 at Brookhaven National Laboratory [72] observed this in e^+e^- pairs (figure 69a). Simultaneously, the SPEAR experiment at SLAC Linear Accelerator Center [73] observed the same peak of events in $e^+e^- \to$ hadrons as well as charged pairs of $e^+e^-, \mu^+\mu^-, \pi^+\pi^-, K^+K^-$ channels.

There's no need for careful statistical analysis to see a great peak at a di-electron mass m_{ee} of around 3.1 GeV in figure 69. This triggered what was known as the November 1974 revolution with the discovery of the charm quark. Soon after, excited states such as the Ψ' were discovered at slightly higher energies.

After spin quantum numbers were measured, we could classify the states analogously to atomic spectroscopy. We can illustrate the energy level diagram for bound states of the charmonium $c\bar{c}$ for the lowest angular momentum states (figure 70).

- The $J/\Psi(3097)$ particle, where the number in the bracket denotes the rest mass $M(c\bar{c})$ in MeV/c^2 is not the lightest $c\bar{c}$ state.
- The lightest state is actually the $\eta_c(2980)$ with $n = 1$ and spin-parity $J^P = 0^-$).
- Instead $J/\Psi(3097)$ is the lightest $n = 1$ with spin-parity of $J^P = 1^-$, exactly that of the photon allowing conservation of angular momentum in the electromagnetic interaction.
- The first excited $n = 2$ bound state of $c\bar{c}$ with spin-parity $J^P = 1^-$, is the $\Psi'(3686)$.

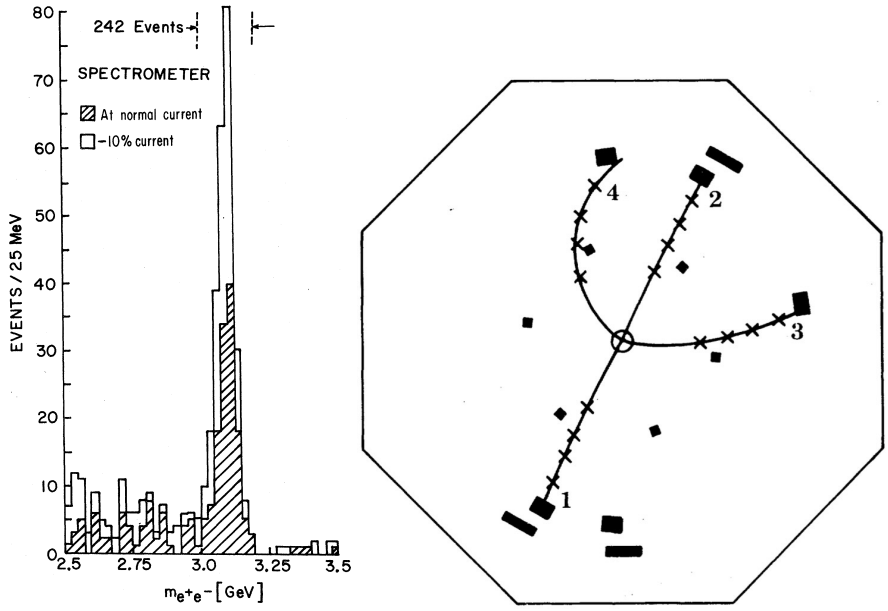

(a) BNL J/ψ [72] (b) $\psi' \to \psi\mu^+\mu^-$ [74]

Figure 69: Discovery of J/ψ and ψ' particles.

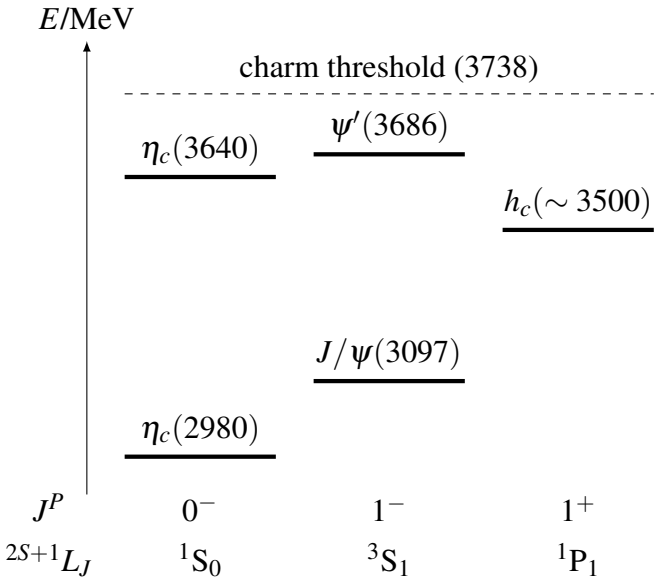

Figure 70: Bound states of charmonium system.

We use the spin-parity J^P notation as well as the spectroscopic notation $^{2S+1}L_J$ alluding to atomic spectra. More energetic states can radiatively decay into lower states via the electromagnetic interaction such as

$$J/\psi(3097) \to \eta_c(2980) + \gamma. \tag{10.39}$$

We discuss the charm threshold below, but we chiefly can understand it as the minimum energy for rapid decays to charmed states.

Bound states of charmonium

We can model the strong interaction between a static quark (coloured) and antiquark (anti-coloured) pair by the potential

$$V(r) = -\frac{4}{3}\frac{\alpha_s \hbar c}{r} + \lambda r \tag{10.40}$$

The first term dominates for distances $r < 0.1$ fm and has a coupling strength α_s given by the strong force analogue of the electromagnetic fine structure constant α_{EM}. Their relative sizes are

$$\frac{\alpha_s}{\alpha_{\text{EM}}} \sim 137$$

The second term dominates for distances $r > 1$ fm with $\lambda \sim 1\,\text{GeV fm}^{-1}$ and offers to explain confinement. Loosely speaking, it models the increasing strength of higher order gluon-gluon interactions that arises as the quark-antiquark pair are pulled apart.

When their separation becomes sufficiently large, it becomes energetically more favourable to produce new quarks from the vacuum rather than increasing $V(r)$ further. These newly formed quarks arrange themselves into colourless hadrons which we observe as narrow cones of jets due to the headlight beaming effect. So this non-vanishing energy as quarks and anti-quarks are drawn apart confines them within hadrons.

We investigate the charm–anti-charm $c\bar{c}$ bound system, known as a **charmonium**, somewhat similar to a hydrogen atom (with proton and electron masses being equal). The charm quarks are sufficiently massive such that much of the bound meson mass is comprised of its quark mass. So we can use the non-relativistic Schrödinger equation to deduce the bound states of the $c\bar{c}$ system. Working in the centre-of-mass frame, we the reduced mass $\mu = m_c/2$ to give

$$\left[-\frac{\nabla^2}{2\mu} + V(r)\right]\Psi(\mathbf{r}) = E\Psi(\mathbf{r})$$

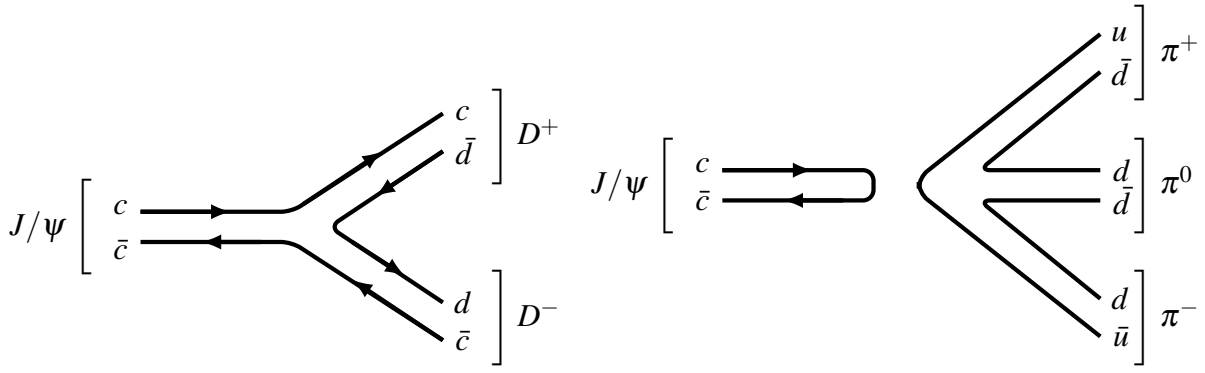

(a) Kinematically forbidden (b) Kinematically allowed but suppressed

Figure 71: Quark-line diagrams for charmonium decays.

Let the binding potential be the $1/r$ dependent first term of (10.40). We should obtain energy spectra analogous to that of hydrogen:

$$E_n = -\frac{\mu}{2}\left(\frac{4\alpha_s}{3}\right)^2 \frac{1}{n^2} \tag{10.41}$$

The resulting bound state masses are then

$$M(c\bar{c}) = 2m_c + E_n. \tag{10.42}$$

Longevity of charmonium

The $J/\Psi(3097)$ state predominantly decays to hadrons with branching ratio of 0.86. Mediated by strong interactions, we expect the decay width to be $\sim$ MeV but instead the measured width is $\approx 90\,\text{keV}$. Figure 71a illustrates the preferred mechanism of decay. The energy $2M_Dc^2$ is the **charm threshold**, as $M_D = 1869\,\text{MeV}/c^2$ is the rest mass of the lightest meson with non-zero charm. Charmonium states heavier than this threshold readily decay into $D^0\bar{D}^0$ or D^+D^- mesons via the strong interaction.

It is tempting to argue the J/ψ can proceed via this diagram in figure 71a. This shows the preferred by the quark lines (only needing one gluon exchange to form the $d\bar{d}$ pair) but it is kinematically forbidden given the $J/\Psi(3097)$ bound state is less than twice the charmed $D^{\pm}(1869)$ meson mass.

Meanwhile the $J/\Psi(3097)$ state $M_{J/\psi} < 2M_D$ is below this threshold. This can only annihilate via the electromagnetic interaction or decay to charmless hadronic states, shown

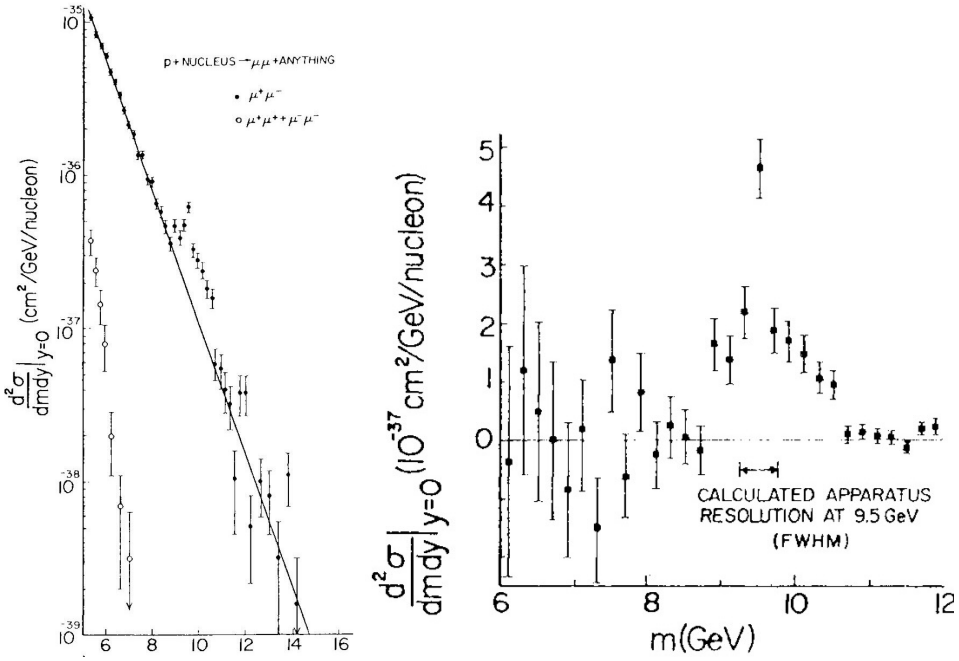

(a) Mass spectrum in GeV (b) Continuum subtracted

Figure 72: Upsilon ($b\bar{b}$) discovered in invariant mass distributions from the 1977 Fermilab E288 experiment. CERN Courier **17** (1977) 7-8

in figure 71b. Kinematically allowed but highly suppressed decay of $J/\psi(3097)$ to charmless π mesons. We understand quark lines being broken between initial and final states are highly suppressed decays, known as OZI suppression. In QCD, we can also understand this as the need for three gluon lines to connect the $c\bar{c}$ to the $u\bar{u}$ and pair of $d\bar{d}$ lines. Historically, this understanding was evidence suggesting the existence of a quark flavour other than u, d, s existing.

An analogous structure of bound states of the bottom quark b known as bottomonium $b\bar{b}$. This was discovered as the Υ meson by the E288 experiment at Fermilab led by Leon Lederman (figure 72). The mass was around 9.46 GeV in dimuon decays and its excited states was discovered a few years later.

11 Quantum chromodynamics

We now discuss empirical evidence for the gauge theory of the strong force: quantum chromodynamics. On first impression, the electromagnetic force and the strong nuclear force could not be more different in nature. Electrodynamics propagates light from the Sun over 150 million miles to our eyes, while jiggling electrons emit light from this screen printing these words. The strong force reveals itself at tiny femtometre distance scales binding protons together and preventing nuclei self-disintegration from electrostatic repulsion.

Though historically far from self-evident, quantum chromodynamics is formally the (non-Abelian) generalisation of quantum electrodynamics. It is a deeply profound and unexpected unification in physics that electromagnetism has a similar mathematical structure as the strong force, and as it turns out the weak force. Indeed, even the gravitational force has a similar structure e.g. the spacetime covariant derivatives in General Relativity.

11.1 Gluons and colour flow

The mediator of the strong force is a spin-one massless boson called the **gluon**. They interact with particles that have colour charge. All quarks carry colour and the fundamental quark-gluon vertex is

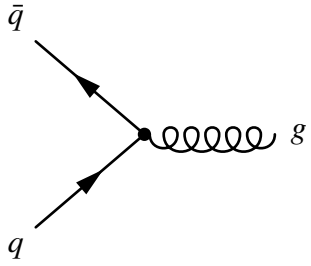

(11.1)

Conventionally, we use a spring to represent the gluon pictorially as a mnemonic for its binding behaviour. The interaction strength of this vertex is given by the strong coupling g_s proportional to the square root of the strong fine structure constant $g_s = \sqrt{4\pi\alpha_s}$, analogous to quantum electrodynamics.

Colour flow

The quark-gluon vertex conserves colour such that all colour charges entering the vertex equals that leaving. Gluons change the colours of participating quarks while leaving their flavour unchanged. We can pictorially represent this in an example involving quark-antiquark annihilation $u\bar{u} \to s\bar{s}$ in its Feynman diagram (left) and corresponding colour flow (right)

representations:

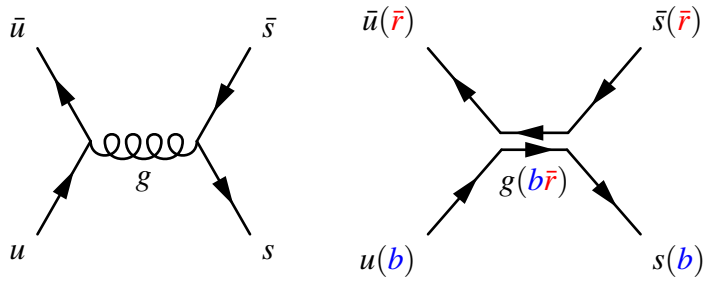

(11.2)

For illustration, we consider an u quark carrying b colour charge and $\bar{u}$ antiquark carrying $\bar{r}$ colour charge. The colour flow is conserved as the gluon carries blue and anti-red charge $g(b\bar{r})$. The quarks retain their respective flavours $u \to u$, $s \to s$ at each vertex, but exchange their colours $r \to b$, $b \to r$. Colour is still conserved at the vertex but the anti-red and blue flow from the individual quarks into the gluon.

Each gluon generally possess colour and anti-colour, and we can conventionally write them as eight linearly independent states:

$$\begin{array}{lll} \frac{1}{\sqrt{2}}(|r\bar{g}\rangle + |\bar{r}g\rangle), & \frac{\mathrm{i}}{\sqrt{2}}(|\bar{r}g\rangle - |r\bar{g}\rangle), & \frac{1}{\sqrt{2}}(|r\bar{r}\rangle + |\bar{b}b\rangle), \\ \frac{1}{\sqrt{2}}(|r\bar{b}\rangle + |\bar{r}b\rangle), & \frac{\mathrm{i}}{\sqrt{2}}(|\bar{r}b\rangle - |r\bar{b}\rangle), & \frac{1}{\sqrt{2}}(|r\bar{r}\rangle + |b\bar{b}\rangle - |g\bar{g}\rangle), \\ \frac{1}{\sqrt{2}}(|g\bar{b}\rangle + |\bar{g}b\rangle), & \frac{\mathrm{i}}{\sqrt{2}}(|\bar{b}g\rangle - 2|b\bar{g}\rangle). & \end{array}$$

We may expect there to be $3 \times 3 = 9$ possible gluon states but one state is colourless:

$$\frac{1}{\sqrt{3}}\left(|r\bar{r}\rangle + |g\bar{g}\rangle + |b\bar{b}\rangle\right).$$

We do not experimentally observe colourless gluons (which would mediate unobserved long-range forces) so we restrict the theory to one that describes nature using the eight independent gluon states with net colour.

A detour on SU(3)

Quantum chromodynamics mathematically represents these eight gluons as a set of unitary 3×3 matrices λ_{ij}^{a} (the a index runs from 1 to 8 for the eight gluons while the ij indices run from 1 to 3 for the three colours) with unit determinant, called the Gell-Mann matrices. At the quark-gluon vertex of a strong interaction (figure 11.2), these gluon matrices act on the quark colours represented by the 3-vector of equation 9.8 as $\lambda_{ij}q_j$. The Gell-Mann matrices are the 3×3 generalisation of the 2×2 Pauli matrices familiar from quantum mechanics describing fermion spin.

Mathematical physicists refer to this group of gluon matrices acting on quark vectors[56] as the 'Special Unitary group of 3-by-3 matrices' i.e. 'SU(3)'. The 'special' refers to the extra condition that the unitary matrices have a real determinant 1 rather than complex $e^{i\phi}$. We say SU(3) is a symmetry because the entire theory of QCD remains unchanged if we swapped the colour labels from red to green, green to blue, and blue to red:

$$|r\rangle \to |g\rangle \to |b\rangle \to |r\rangle; \quad \text{theory remains invariant.} \tag{11.3}$$

The mathematics of *Lie Groups* underpin this description of SU(3), which are further elaborated in group theory and quantum field theory classes, but this miniature technical detour hopefully gives a heuristic of why particle physicists refer to the strong force by 'SU(3)'.

11.2 Evidence for three colours

Among the definitive evidence for the quark model and the existence of three colour states is found by considering the ratio

$$R = \frac{\sigma(e^+e^- \to \text{hadrons})}{\sigma(e^+e^- \to \mu^+\mu^-)}, \tag{11.4}$$

as a function of centre-of-mass energy $\sqrt{s}$. From our understanding of electromagnetic scattering, the vertex factor contributes a the electric charge Q_i^2 for the final-state quarks and muons involved

$$R = \frac{\sigma_{\text{hadrons}}}{\sigma_{\text{muons}}} = \frac{\sum_i Q_i^2}{Q^2_{\mu^+\mu^-}}. \tag{11.5}$$

At large energies the density of states factor for both cross-sections are nearly equal, so this ratio is well-approximated by

$$R = \frac{Q^2_{u\bar{u}} + Q^2_{d\bar{d}} + Q^2_{s\bar{s}} + Q^2_{c\bar{c}} + Q^2_{b\bar{b}}}{Q^2_{\mu^+\mu^-}} = \left(\frac{2}{3}\right)^2 + \left(-\frac{1}{3}\right)^2 + \left(-\frac{1}{3}\right)^2 + \left(\frac{2}{3}\right)^2 + \left(-\frac{1}{3}\right)^2. \tag{11.6}$$

This gives our theoretical prediction of the ratio for 5 quarks as

$$R_{\text{the}} = \frac{11}{9}. \tag{11.7}$$

Now we compare with experimental data (figure 73). Below $\sqrt{s} \sim 4\,\text{GeV}$, we have only sufficient energies for up, down and strange quark pair production $e^+e^- \to u\bar{u}, d\bar{d}, s\bar{s}$. For

[56] Formally, the gluon matrices are in the *adjoint representation* while the (anti)quarks vectors are in the *(anti)fundamental representation* of SU(3).

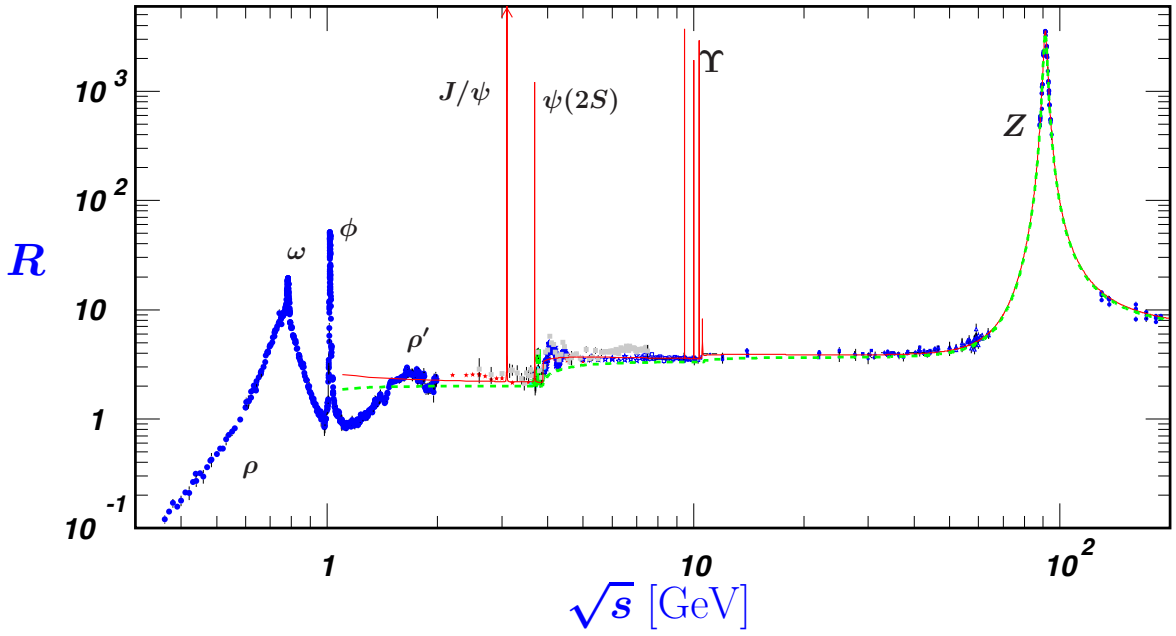

Figure 73: Ratio of the branching ratios of electron position annihilation to hadrons and muons $R = \sigma(ee \to \text{hadrons})/\sigma(ee \to \mu\mu)$. Reproduced from Particle Data Group [75].

$4 < \sqrt{s} < 10\,\text{GeV}$ we reach the kinematic threshold for the charm quark $e^+e^- \to c\bar{c}$, which adds to the rate of total hadron production. Above $\sqrt{s} \approx 10$ GeV, we reach the threshold for production of the bottom quark pair production $e^+e^- \to b\bar{b}$. Experiment finds

$$R_{\text{exp}} \approx 3 \tag{11.8}$$

for $\sqrt{s} > 4\,\text{GeV}$ sufficient for production of charm/bottom quark. There is a discrepancy between the theoretical and experimental ratio R of about a factor of 3. This suggests there exists 3 additional degrees of freedom left unaccounted in our model of quarks. This is strong evidence for colour.

11.3 Yang–Mills theory

This is a brief review of Yang–Mills theory applied to QCD, which those taking QFT classes will study in greater mathematical detail. The strong force is analogous to QED, extending the local symmetry from U(1) $e^{iI\alpha(x)}$ with the 1×1 unitary matrix (the identity I) to 3×3 unitary matrices t_a, the SU(3) group. The photon four-potential $A_\mu(x)$ extends to the gluon potential $t_a G^a_\mu$ with these eight 3×3 matrices attached to it. The corresponding QCD

covariant derivative extends the QED covariant (4.41) derivative to become:

$$\partial_\mu \to D_\mu = \partial_\mu + \mathrm{i} g_s t_a G^a_\mu, \tag{11.9}$$

where g_s is the dimensionless strong coupling and $t_a = \lambda_a/2$, with λ_a being the Gell-Mann matrices. For completeness, we print these matrices in a particular basis to look at:

$$\begin{aligned}
\lambda_1 &= \begin{pmatrix} 0 & 1 & 0 \\ 1 & 0 & 0 \\ 0 & 0 & 0 \end{pmatrix}, \quad \lambda_2 = \begin{pmatrix} 0 & -\mathrm{i} & 0 \\ \mathrm{i} & 0 & 0 \\ 0 & 0 & 0 \end{pmatrix}, \quad \lambda_3 = \begin{pmatrix} 1 & 0 & 0 \\ 0 & 1 & 0 \\ 0 & 0 & 0 \end{pmatrix}, \\
\lambda_4 &= \begin{pmatrix} 0 & 0 & 1 \\ 0 & 0 & 0 \\ 1 & 0 & 0 \end{pmatrix}, \quad \lambda_5 = \begin{pmatrix} 0 & 0 & -\mathrm{i} \\ 0 & 0 & 0 \\ \mathrm{i} & 0 & 0 \end{pmatrix}, \quad \lambda_6 = \begin{pmatrix} 0 & 0 & 0 \\ 0 & 0 & 1 \\ 0 & 1 & 0 \end{pmatrix}, \\
\lambda_7 &= \begin{pmatrix} 0 & 0 & 0 \\ 0 & 0 & -\mathrm{i} \\ 0 & \mathrm{i} & 0 \end{pmatrix}, \quad \lambda_8 = \frac{1}{\sqrt{3}} \begin{pmatrix} 1 & 0 & 0 \\ 0 & 1 & 0 \\ 0 & 0 & -2 \end{pmatrix}.
\end{aligned} \tag{11.10}$$

You can see the first three are precisely the Pauli matrices describing SU(2) in the upper-left corner. These matrices obey the algebra $[t_a, t_b] = \mathrm{i} f_{abc} t_c$ involving the SU(3) structure functions f_{abc}. The covariant derivative acts non-trivially on the quark Dirac spinors $q_i(x)$, which experience the local transformation transform

$$q_i(x) \to q'_i(x) = \exp\left[\mathrm{i} g_s (\lambda^a_{ij}/2) G^a_\mu(x)\right] q_j(x). \tag{11.11}$$

There is quite a large number of indices to keep track of here, which we can walk through in turn:

- **Lorentz** $\mu = \{0,1,2,3\}$: this runs over the Lorentz four-vector index;
- **Gluon** $a = \{1,2,\ldots,8\}$: this runs over the eight Gell-Mann matrices corresponding to the eight gluons in nature. In group theory language, gluons are described by the *adjoint representation* of SU(3);
- **Colour** $i, j = \{1,2,3\}$: this runs over the elements of the 3×3 matrices, which we can interpret as the colours of the quarks. In group theory language, quarks are described by the *fundamental representation* of SU(3);
- **Flavour** $q = \{u,d,s,c,b,t\}$: this runs over the six quark flavours in nature.
- **Spinor**: we have suppressed the four Dirac spinor indices on the quarks that the γ^μ matrices act on.

The gluon field strength $G_{\mu\nu} = t_a G^a_{\mu\nu}$ has a similar structure to the electromagnetic field strength $F_{\mu\nu}$

$$G_{\mu\nu} = \frac{1}{\mathrm{i}g_s}[D_\mu, D_\nu] = \partial_\mu G_\nu - \partial_\nu G_\mu + \mathrm{i}g_s[t_b G^b_\mu, t_c G^c_\nu]. \tag{11.12}$$

The non-commuting t_a matrices gives an extra bit involving the SU(3) structure functions, which we can write as

$$G^a_{\mu\nu} = \partial_\mu G^a_\nu - \partial_\nu G^a_\mu - g_s f^{abc} G^b_\mu G^c_\nu. \tag{11.13}$$

Under a gauge transformation, the gauge function acquires an extra non-commuting term relative to how this worked for the photon field A_μ:

$$G^a_\mu \to \tilde{G}^a_\mu = G^a_\mu - \chi^a_\mu, \quad \chi^a_\mu = \partial_\mu \Lambda^a + g_s f^{abc} \Lambda^b G^c_\mu. \tag{11.14}$$

The kinetic term in the Lagrangian governing the motion of gluon fields is given by

$$\mathscr{L}^{\text{kinetic}}_{\text{gluon}} = -\frac{1}{2}\mathrm{tr}\left(G_{\mu\nu}G^{\mu\nu}\right) = -\frac{1}{4}G^a_{\mu\nu}G^{\mu\nu}_a, \tag{11.15}$$

using the fact the t_a matrices conventionally satisfy the trace relation $\mathrm{tr}(t_a t_b) = \frac{1}{2}\delta_{ab}$. Combining this with the Dirac Lagrangian term for quarks, this gives the QCD Lagrangian governing the interactions of quarks and gluon:

$$\boxed{\mathscr{L}_{\text{QCD}} = -\frac{1}{4}G^a_{\mu\nu}G^{\mu\nu}_a + \mathrm{i}\bar{q}\gamma^\mu(\partial_\mu + \mathrm{i}g_s t_a G^a_{\mu\nu})q.} \tag{11.16}$$

The quantisation and renormalisation of this Lagrangian and non-Abelian gauge theories are rather complicated, to use some understatement, due to the non-propagating gauge degrees of freedom. Showing this is well beyond the scope of this class, but the crucial breakthroughs of Veltmann and 't Hooft in the 1970s demonstrated QCD was a viable theory of nature.

The extra term given by the non-commuting gluon fields $g_s f^{abc} G^b_\mu G^c_\nu$ is makes QCD a **non-Abelian gauge theory** and is a hallmark of Yang–Mills theory. This non-commuting term endows QCD with qualitative phenomenological differences compared to the Abelia gauge theory of QED. Expanding out the kinetic Lagrangian gives terms that feature three $\sim GG(\partial G)$ and four $\sim GGGG$ gluon fields. This implies the existence of gluon self-interactions at tree-level shown in figure 74. This is related to the fact that gluons have non-zero net colour. They feel the strong force and can therefore interact with other gluons. This contrasts with photons carrying no electric charge and have no self-interactions at tree-level. Gluons can therefore source other gluons under the strong interaction, and offers an explanation for confinement.

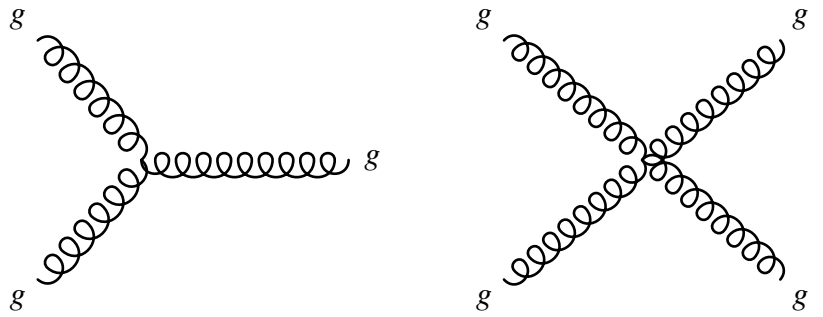

(a) 3 gluon vertex (b) 4 gluon vertex

Figure 74: Gluon self-interaction vertices due to the non-Abelian structure of quantum chromodynamics.

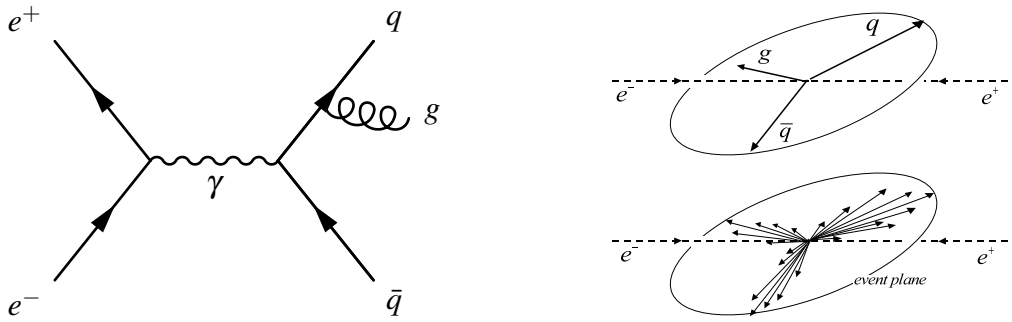

(a) Feynman diagram (b) Planarity of three jets [76]

Figure 75: Diagrams for the gluon bremsstrahlung discovery process $e^-e^+ \to q\bar{q}g$.

11.4 Asymptotic freedom

The gluon was discovered in 1979 via the gluon bremsstrahlung process (figure 75a). A distinctive feature of these events was that all three jets resulting from the quarks and gluon are approximately coplanar due to momentum conservation (figure 75b). The four experimental collaborations at PETRA in DESY, Hamburg (figure 34a) sought evidence for this process, which was promptly observed by all four experiments (figure 76a).

In 1972, the renormalisation of QCD was completed by 't Hooft and Veltman. Then Politzer, Gross and Wilczek calculated the beta function of QCD in 1973 and discovered it decreased with energy scales.

The strong force coupling α_{QCD} in quantum chromodynamics decreases with energy scale. It is more difficult to draw pretty pictures for why this happens, but some texts discuss a concept of "anti-screening". The QCD beta function, in terms of the number of active

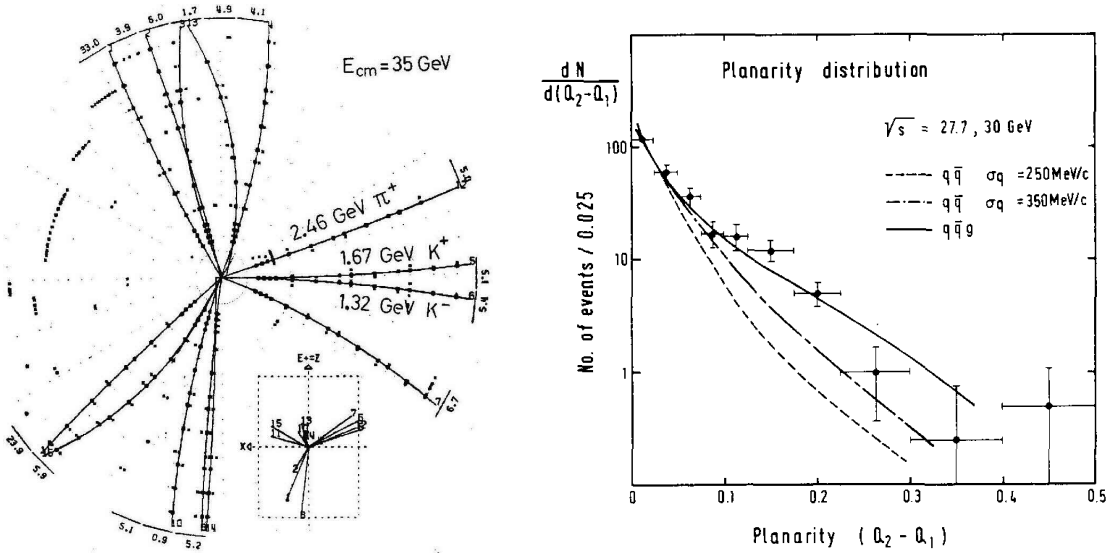

(a) TASSO three-jet event (b) JADE data on qqg [77]

Figure 76: Discovery of gluon in $ee \to qqg$ three-jet events.

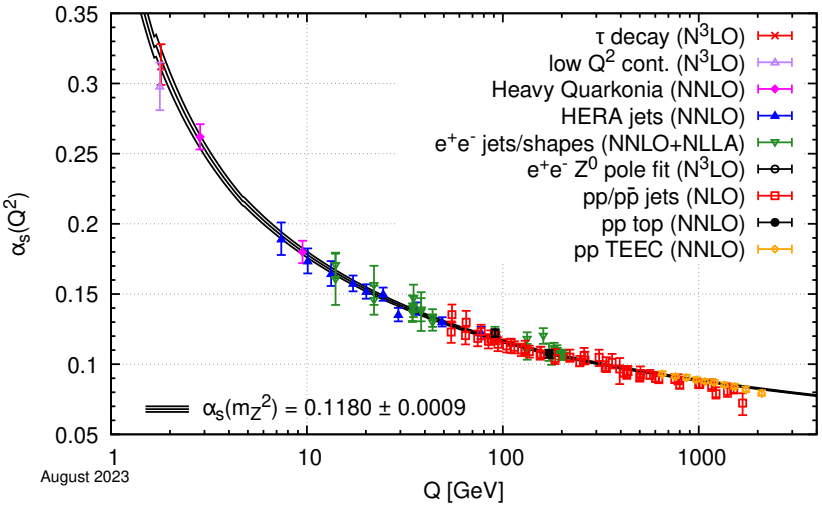

Figure 77: **Running of strong coupling**. Displayed is the strong coupling $\alpha_s(Q^2)$ as a function of momentum transfer Q^2 from Ref. [75]. The measurements are performed using various probes, and the line shows the five-loop running taking $\alpha_s(m_Z^2) = 0.1180 \pm 0.0009$ as input.

flavours N_f with colour charge, is:

$$\beta(\alpha_{\text{QCD}}) = -\left(33 - 2N_f\right)\frac{\alpha_{\text{QCD}}^2}{6\pi}. \tag{11.17}$$

In the Standard Model, $N_f = 6$, giving a negative beta function. The measured values at various Q^2 are summarised figure 77.

One conceptually simple way to probe this is to measure the ratio of three-jet to two-jet events:

$$R_{32} = \frac{\sigma(ee \to qqg)}{\sigma(ee \to qq)} \propto \alpha_s(Q), \tag{11.18}$$

where $Q = \frac{1}{2}(p_{\mathrm{T}}^{j1} + p_{\mathrm{T}}^{j2})$ is the average transverse momentum of the two jets with the highest p_{T}. This can be extended to hadron colliders, where CMS made among the first measurements out to $Q \approx 900$ GeV in 2013 [78]. At hadron colliders, there are more diagrams such as gluon scattering to consider.